SANDIA REPORT
SAND2024-12991R
Printed September 2024

Sandia National Laboratories

Characterizing the effect of hypersonic boundary layer turbulence on antenna performance: A computational approach

Nicholas A. Roberds
Matthew W. Young
Nathan E. Miller
Caleb Logemann

Prepared by
Sandia National Laboratories
Albuquerque, New Mexico 87185
Livermore, California 94550

Issued by Sandia National Laboratories, operated for the United States Department of Energy by National Technology & Engineering Solutions of Sandia, LLC.

NOTICE: This report was prepared as an account of work sponsored by an agency of the United States Government. Neither the United States Government, nor any agency thereof, nor any of their employees, nor any of their contractors, subcontractors, or their employees, make any warranty, express or implied, or assume any legal liability or responsibility for the accuracy, completeness, or usefulness of any information, apparatus, product, or process disclosed, or represent that its use would not infringe privately owned rights. Reference herein to any specific commercial product, process, or service by trade name, trademark, manufacturer, or otherwise, does not necessarily constitute or imply its endorsement, recommendation, or favoring by the United States Government, any agency thereof, or any of their contractors or subcontractors. The views and opinions expressed herein do not necessarily state or reflect those of the United States Government, any agency thereof, or any of their contractors.

Printed in the United States of America. This report has been reproduced directly from the best available copy.

Available to DOE and DOE contractors from

U.S. Department of Energy
Office of Scientific and Technical Information
P.O. Box 62
Oak Ridge, TN 37831

Telephone: (865) 576-8401
Facsimile: (865) 576-5728
E-Mail: reports@osti.gov
Online ordering: http://www.osti.gov/scitech

Available to the public from

U.S. Department of Commerce
National Technical Information Service
5301 Shawnee Road
Alexandria, VA 22312

Telephone: (800) 553-6847
Facsimile: (703) 605-6900
E-Mail: orders@ntis.gov
Online order: https://classic.ntis.gov/help/order-methods

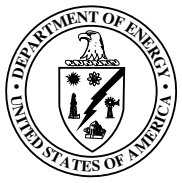

ABSTRACT

The degradation of antenna performance during hypersonic re-entry is a well known phenomenon that can lead to complete radio blackout. Recent additions to the Empire code establish it as a tool for the study and analysis of the problem. Coupling to the Sandia Parallel Aerodynamics and Reentry Code (SPARC) enables the electromagnetic analysis of realistic re-entry plasma profiles. The geometric flexibility afforded by both Empire and SPARC allow the consideration of arbitrary vehicle and antenna configurations. We have used this tool to study antenna performance during re-entry when the boundary layer becomes turbulent. A concise description of line-of-sight transmissions, which employs advanced statistical methods, was developed. New insights into the low altitude reflectometer readings of RAM-C2 are offered. Techniques for the reconstruction of the re-entry plasma profile from reflectometer data were explored.

This page intentionally left blank.

ACKNOWLEDGEMENT

The contributions of Ross Wagnild and Tony Statom were greatly appreciated in this effort.

This page intentionally left blank.

CONTENTS

This page intentionally left blank.

LIST OF FIGURES

LIST OF TABLES

This page intentionally left blank.

1. INTRODUCTION

An aircraft or spacecraft, transiting through the atmosphere at a hypersonic velocity, may be enveloped by a plasma layer due to extreme compressive and viscous heating of the air. It is well known that re-entry plasma layers can disrupt the operation of any onboard antennas. The space shuttle experienced communications blackout [1] between 265 and 162 kft altitude, lasting sixteen minutes.

In the electromagnetic analysis of a re-entry plasma, the appropriate model is an isotropic, linear cold plasma. The relative electric permittivity is,

$$\epsilon_r = 1 - \frac{\omega_\mathrm{p}^2}{\omega(\omega - i\nu)}, \tag{1.1}$$

where ω is the electromagnetic signal angular frequency and ν is the electron collision frequency. The plasma frequency,

$$\omega_\mathrm{p} = \sqrt{\frac{n_\mathrm{e} e^2}{m_\mathrm{e}\epsilon_0}}, \tag{1.2}$$

is proportional to the square root of the electron density n_e. Here, e is the elementary charge, m_e is the electron mass and ϵ_0 is the electric permittivity. This model, which is sometimes called the Drude model, assumes the absence of strong, applied magnetic fields or very high electromagnetic signal power which would introduce nonlinearity.

Given the electron density and collision frequency profile of the re-entry plasma, there is a hierarchy of approaches for understanding the performance degradation that an antenna will experience. Let us start with the simplest, which is to just compare the signal frequency, ω, to the peak plasma frequency in the plasma profile, ω_p. Electromagnetic waves in an unmagnetized, linear plasma have the same [2] dispersion relation as O-waves. For $\omega \gg \omega_p$, there is little interaction with the plasma; microwave signals will pass through the plasma unaffected. For signal frequencies $\omega \lesssim \omega_p$, the interaction with the plasma cannot be neglected and a higher fidelity approach is required to better understand what impacts on antenna performance can be expected.

At the next level of fidelity, we can consider the homogeneous plasma slab model, where an electromagnetic plane wave is normally incident on a slab of finite thickness. Solutions[1] to the slab model yield a transmission coefficient and a reflection coefficient. We can gain some intuition about the problem by considering the solutions to some slabs with $\omega_p = 5$ GHz, shown in Fig. 1-1. The slab problem parameters are scanned to show the impact of different slab thicknesses Δx and plasma collision frequencies ν on the transmission coefficient. In all cases, the transmission coefficient falls off at low frequencies below ω_p. The falloff in transmission coefficient is smoothed about ω_p for a larger collision frequency ν.

[1] The homogeneous plasma slab model has an analytic solution that is amenable to a pen-and-paper approach.

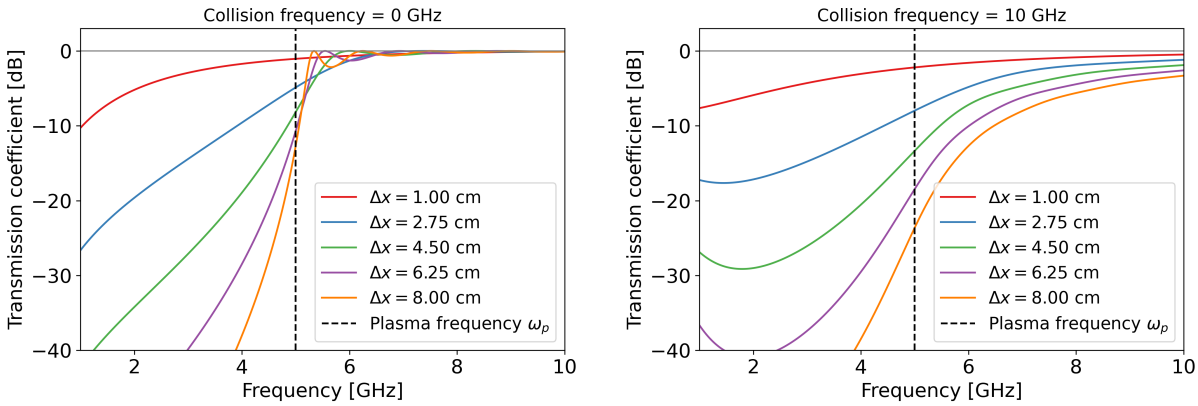

Figure 1-1. The transmission coefficient for the homogeneous plasma slab problem, for various slab thicknesses Δx. The electron collision frequency is zero in (a) and 10 GHz in (b) and in all cases the plasma frequency is 5 GHz. Attenuation is greatly reduced for microwave frequencies above the plasma frequency in all cases. The effect of varying the slab thickness or collision frequency is significant.

The next higher fidelity model would be the inhomogeneous plasma slab model. A solution to this model can be obtained by considering the inhomogeneous slab to be an arrangement of thin homogenous slabs. The coupling between adjacent slabs can be represented by the same linear system as the homogeneous slab model; the usual solution technique is called the *transmission matrix method*. A study by Statom [3] has provided some detailed characterization of (homogeneous and inhomogenous) plasma slab responses.

In many cases, the humble plasma slab model provides an excellent approximation and more sophisticated models may not be worth the effort. However, in this report, we will see many situations where a simple slab model will not suffice for even a qualitative understanding of antenna performance. For example, a one-dimensional model will, in general, yield a completely different antenna reflection coefficient compared to a 3D model because it cannot account for surface wave excitation. In the case that the boundary layer is turbulent, a 1D model will fail to account for the depolarization of the signal which can be quite significant for realistic flows having an anisotropic structure. An interpretation of the results in section 4 indicates that a one-dimensional model will fail to recover the correct statistical properties of the signal amplitude fluctuations for the case of a turbulent re-entry plasma.

Capabilities recently added to the Empire plasma code [4] allow for much higher fidelity models of antenna/re-entry plasma layer interactions. Empire is a finite element time-domain code, allowing a great deal of flexibility in the specification of the antenna, aircraft structure and plasma layer[2]. Support for linear material models, including the isotropic linear plasma dielectric (Eq. 1.1) and plasma-matched open boundary conditions have been added. Diagnostics for computing the far fields and S-parameters are now provided. At least half of the effort in estimating re-entry performance is in determining the plasma profile. In Empire, the plasma profile can now be loaded from the Sandia Parallel Reentry Code (SPARC) output, or specified with an arbitrarily long analytic expression. SPARC [5] is a cutting edge code for computing hypersonic flow solutions. In chapter

[2]Empire can, of course, solve homogeneous or inhomogeneous plasma slab problems as well

2, these new Empire capabilities are described in detail.

We used this new capability to conduct analyses of antenna performance in re-entry conditions, especially for situations where the boundary layer is turbulent. All of the analyses are based on the RAM-C2 experiment [6, 7, 8]. The RAM (Radio Attenuation Measurements) experiments, conducted in the 1960s, gathered data on re-entry plasmas and their effect on antenna performance. The RAM-C series ballistic vehicles were spherically blunted cones with nose diameter, $d_{\mathrm{N}} = 12$ in.

Section 3 presents an analysis showing how an antenna responds to the presence of a re-entry plasma. A realistic model of the RAM-C aft X-band reflectometer, informed by the published schematics, was considered. Changes in the far field pattern and shifts in the tuning (S-parameter resonances) are presented and discussed.

When the boundary layer is turbulent, transmitted and reflected microwave signals are subject to a *parasitic modulation*. The amplitude and phase fluctuate at high frequencies (tens to hundreds of kilohertz). A great deal of information about this parasitic modulation of the signal can be communicated concisely and quantitatively. This is the subject of section 4.

In the historical RAM-C2 flight, interesting measurements were recorded by the reflectometers at low altitudes. Investigators connected the phenomenon to a transition to boundary layer turbulence, and suggested [6] reflectometry as a diagnostic for detecting boundary layer transition. In section 5, a picture which potentially explains these historical observations emerges from Empire electromagnetic analysis of SPARC calculations.

Reflectometry is a diagnostic technique rarely used in space research, despite its prominent role in the famous RAM-C experiments. The technology has been mostly developed by the magnetic confinement fusion community. In section 6, we engage in a study of reflectometry techniques for reconstructing re-entry plasma profiles.

This page intentionally left blank.

2. RE-ENTRY ANTENNA PERFORMANCE MODELING WITH EMPIRE

Empire implements a finite element time-domain (FETD) method for electromagnetics. The flexibility in problem geometry and mesh arrangement afforded by FETD allows for virtually unconstrained specifications of vehicle geometries and antenna configurations. With the time-domain approach, each simulation provides results for a range of frequencies, which is convenient for our main topic: characterizing antenna performance when the boundary layer is turbulent.

Empire uses conforming finite element basis functions to facilitate the $\nabla \cdot \boldsymbol{B} = 0$ constraint. In particular, the electric field $\boldsymbol{E}$ discretized on mesh edges using lowest order Nedéléc elements of the first kind [9] and the magnetic field $\boldsymbol{H}$ discretized on mesh faces using lowest order Raviart-Thomas elements [10].

Several new capabilities were added to Empire for analyzing re-entry antenna performance. We added support for linear material models in Empire electromagnetics. Arbitrary electron density and collision frequency fields can be specified to inform the linear plasma model Eq. 1.1. Also, a perfectly matched layer (PML) boundary condition, formulated as a linear material model, is now available. PML matching to vacuum or to a specified linear plasma profile is supported. Details regarding the linear plasma model formulation and implementation are given in Appendix A. The development of these capabilities required a deep understanding of the Empire electromagnetic solver formulation and organization, but this has not been communicated in significant detail anywhere. A detailed account of the Empire electromagnetic method is given in Appendix B. Some recent papers [11, 12] by Empire team members provide additional insight as well.

We also added the capability to load a plasma profile from the output of the SPARC hypersonic flow code onto the Empire finite elements. Alternatively, the user can specify an analytic expression for the plasma profile (say, a bigaussian function [13] or some series representation). Loading from SPARC is achieved by Galerkin projection. A detailed account of the method is given in our recent paper [14]. A key element is the use of the R3D library [15] to compute intersections of the Empire hexahedral or tetrahedral elements with the CGNS mesh elements that come from SPARC. Recursive octree partitioning of the domain is used to minimize the number of R3D intersection calculations required, so loading takes only a small fraction of the total simulation time.

New Empire diagnostics providing both frequency-domain and time-domain near to far field transformations (NTFFs) allow the user to estimate the far field response from a calculation of the near field evolution. While frequency-domain NTFF diagnostics are quite common in electromagnetic codes, a time-domain NTFF is somewhat more unusual, although it allows more efficient use of Empire's time-domain calculation in many cases. Some time-domain NTFF methods for finite difference time-domain (FDTD) codes have appeared in the literature [16, 17, 18, 19, 20]. However, we could not find any published NTFF methods for conforming FETD codes. Therefore, we had to

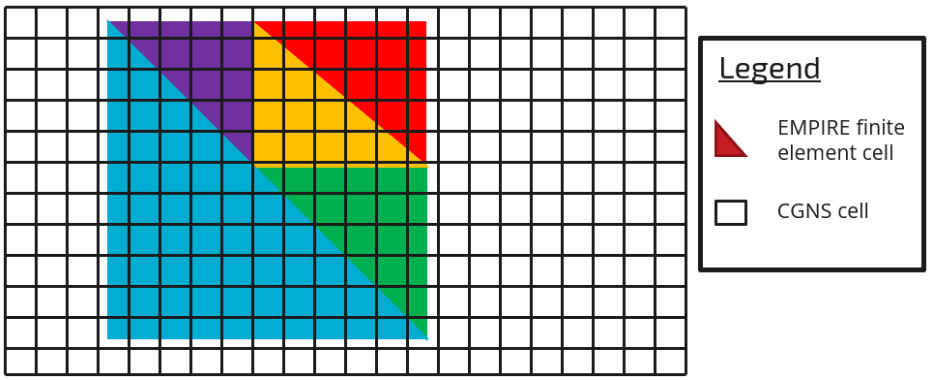

Figure 2-1. Coupling SPARC and Empire: We use Galerkin projection of the SPARC solution onto the Empire finite elements. The R3D library is utilized for computing the intersections between SPARC and Empire grid cells after an octree decomposition of the domain.

formulate a new time-domain NTFF method for Empire. Our method addresses certain non-trivial difficulties with computing the NTFF in a conforming finite element code.

Development of the NTFF method was driven by a novel benchmark verification problem. Historically, scattering problems (e.g. the Mie sphere problem) have been used to verify NTFF method implementations. However, Empire is not equipped for scattering problems and so it was necessary to formulate a novel benchmark problem. The benchmark is a magnetic quadrupole expansion problem, formulated so that the NTFF operates on fields with a near zone character (where the electric and magnetic fields are out of phase and have significant radial components) and the NTFF result can be compared to an exact result that was obtained by an asymptotic matching procedure. Our time-domain NTFF method for conforming FETD codes and the benchmark problem formulation are currently under review for publication [21]. We note that the correctness and accuracy of the NTFF diagnostics is essential for hypersonic antenna problems; the far fields are the primary quantity of interest in many or perhaps most such analyses.

We developed postprocessing scripts which can compute the scattering parameters (S-parameters) between different radio frequency (RF) ports. In this case, RF ports correspond to Empire port boundary conditions (sometimes referred to as "TLBC" boundary conditions within the Empire user community). Scattering parameters are of great interest in the study of antenna performance in the hypersonic environment. The presence of a nearby plasma layer can generally be expected to alter the tuning of an antenna.

The scripts *ScatteringParametersFourier.py* and *ScatteringParametersDirect.py* implement different methods for computing the scattering parameters. The Fourier method requires the 1D output from the port boundary condition at every time step[1]. The forwards and backwards moving waves are deconvolved from this data using a 2D FFT. Then it reconstructs the dispersion relation $k(\omega)$ and port impedance $Z(\omega)$. The direct method requires the incident wave, dispersion relation and port impedance to be given by the user. With this information, the forward and backwards power

[1]This amounts to hundreds of kilobytes of data for a typical run.

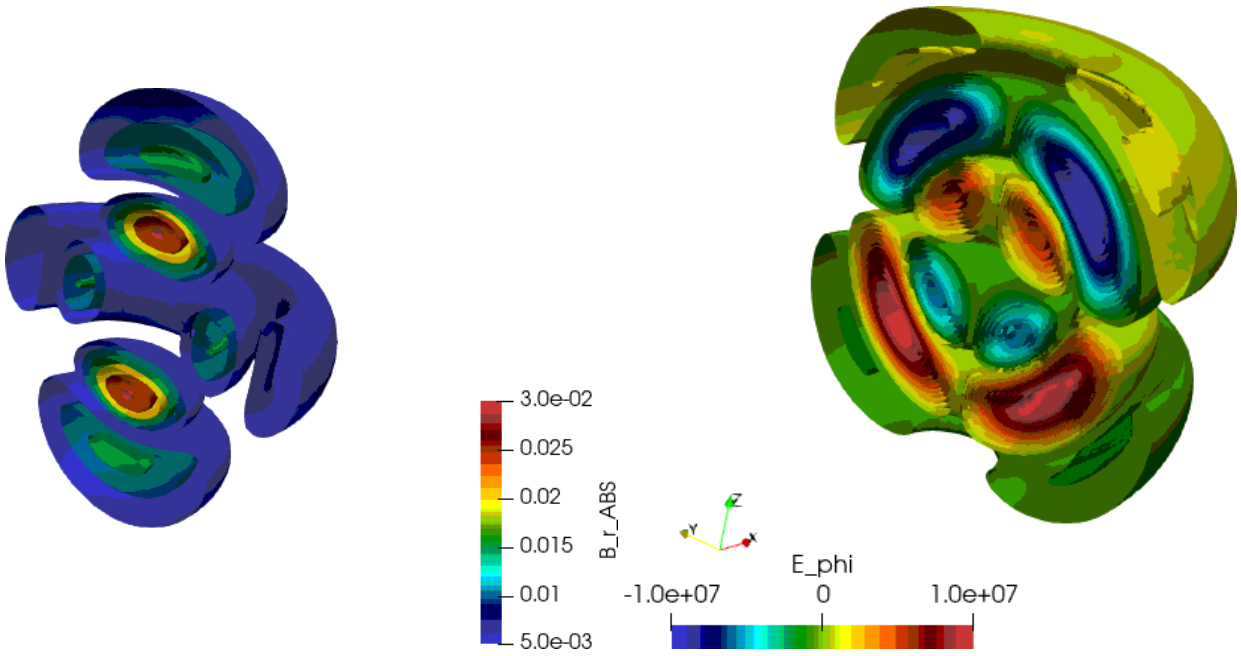

Figure 2-2. Electric and magnetic fields for a solution of the near to far field transformation (NTFF) benchmark verification problem. Development of this benchmark problem was necessary towards formulating a correct and accurate NTFF diagnostic.

waves for each port i can be computed,

$$a_i(\omega) = \frac{U_{i,\mathrm{f}}(\omega)}{\sqrt{Z_i(\omega)}} \tag{2.1}$$

$$b_i(\omega) = \frac{U_{i,\mathrm{r}}(\omega)}{\sqrt{Z_i(\omega)}} \tag{2.2}$$

where $U_{i,\mathrm{f}}$ and $U_{i,\mathrm{r}}$ are the forward and backwards traveling voltage waves, respectively. Then the scattering parameters,

$$S_{ij}(\omega) = \frac{b_j}{a_i}. \tag{2.3}$$

$$\tag{2.4}$$

The result of a simple coaxial cable benchmark problem, which is used as a verification test, is given in Fig. 2-3.

Besides the simple coaxial cable benchmark problem, we attempted some cross-code validation by comparing our S-parameter results to results from Ansys HFSS for non-trivial antenna structures. Our finding was that achieving good agreement with HFSS can be challenging and requires very careful construction of the Empire computational mesh. This is due to the use of low order electromagnetics in Empire (first order spatial discretization). We observed that Empire hexahedral meshes give a much better result compared to unstructured tetrahedral meshes at a given level of mesh refinement.

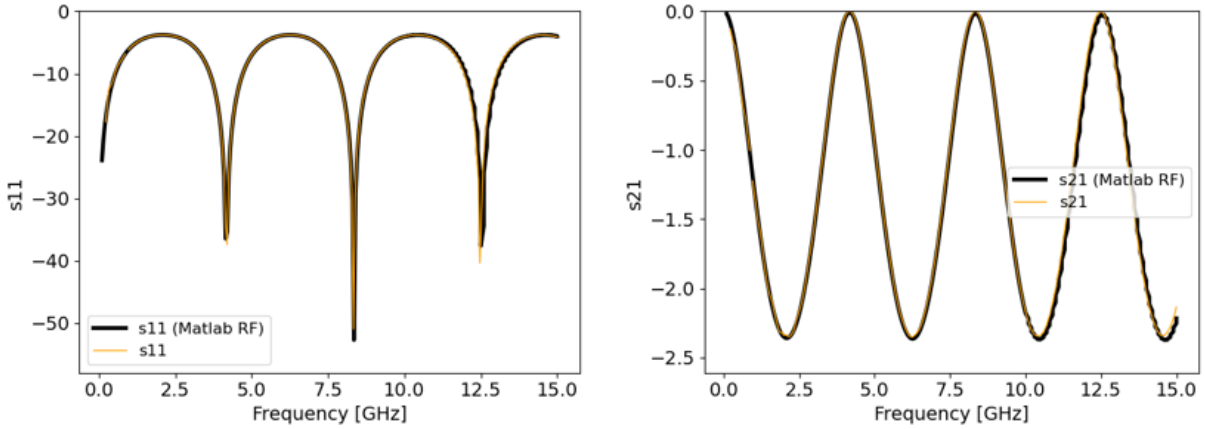

Figure 2-3. Scattering parameters, for a simple coaxial benchmark problem, computed using the new Empire postprocessing S-parameter script (Fourier method). The reference solution was computed with Matlab RF.

3. REALISTIC MODEL OF A RAM-C2 X-BAND REFLECTOMETER ANTENNA

We can use the flexibility in problem geometry afforded by the Empire finite element method to calculate the behavior of a realistic model for the RAM-C2 aft X-band antenna under re-entry conditions. A detailed schematic of the antenna is documented by Grantham [8]: it was a conical horn coupled to an impedance matched coaxial cable transition.

The Empire problem domain can be discussed in terms of four distinct regions. There is the coax-to-horn transition region, horn antenna structure, the 1/3 in thick teflon heat shield and the outside region which includes the re-entry plasma. They are depicted in Fig. 3-1 (a), along with an indication of the plasma density in the outside region. Although it cannot be discerned in the figure, a teflon plug extends roughly 3 cm into the horn structure from the teflon heat shield region.

The plasma profile at the aft X-band antenna, for several altitudes during the RAM-C2 re-entry, is shown in Fig. 3-1 (b). For this analysis, we'll consider the situation at 40 km. We used a uniform electron collision frequency model.

The simulation procedure is to ring the antenna with a sine-modulated Gaussian pulse signal. This is accomplished with the port boundary condition terminating the coax. The parameters of the pulse are chosen to excite some frequency band of interest; a shorter pulse width will excite a broader range of frequencies, with the central frequency determined by the sine modulation. The simulation is then run until the energy is completely dissipated. With the diagnostics and postprocessing techniques outlined in section 2, the frequency-dependent properties of the antenna performance can be extracted from the raw solution result.

From the perspective of electromagnetic signal propagation, there are several critical transitions that occur along the path of the signal. These transitions include the coax to horn transition, the interface between the horn antenna and the heat shield and the interface between the heat shield and the atmosphere. Each of these transitions introduces reflections associated with their impedance mismatch [22]. Ultimately, some of the transmitted microwave energy is reflected back into the coax.

The reflection coefficient, $S_{11}(\omega)$, is the ratio of the backwards traveling wave in the coax to the transmitted wave. The reflection coefficient is directly affected by the presence and characteristics of the re-entry plasma. As the plasma properties vary with re-entry conditions, the amplitude and phase of S_{11} evolves. That is, the re-entry plasma dynamically changes the tuning of the antenna system.

We computed the reflection coefficient for the 40 km re-entry plasma as well as the vacuum situation (no plasma) using the S-parameter extraction techniques from Section 2. The result is shown in Fig. 3-2 (a). Especially at lower frequencies, near the profile peak plasma frequency of 9 GHz,

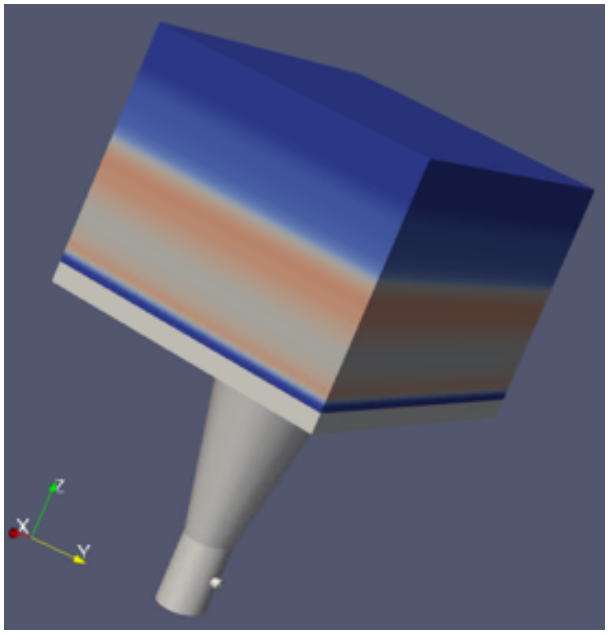

(a) Plot of the Empire problem domain. The plasma electron density in the outer region, corresponding to RAM-C2 conditions at 40 km altitude, is indicated by the coloring. The teflon heat shield, horn antenna and coax transition regions are indicated in the solid grey color.

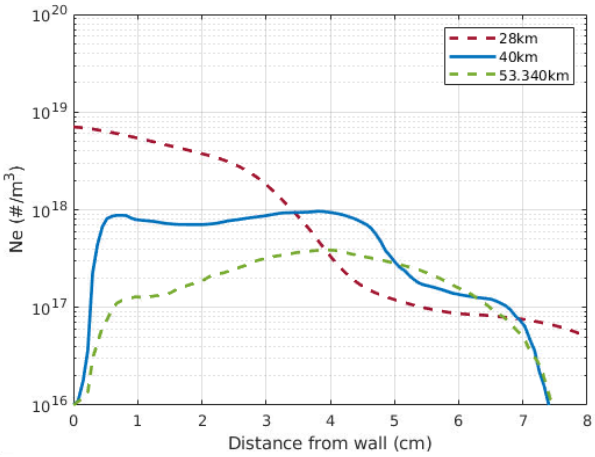

(b) Plasma profile at the aft X-band reflectometer for several altitudes during re-entry.

Figure 3-1. The geometry and plasma profile for the problem.

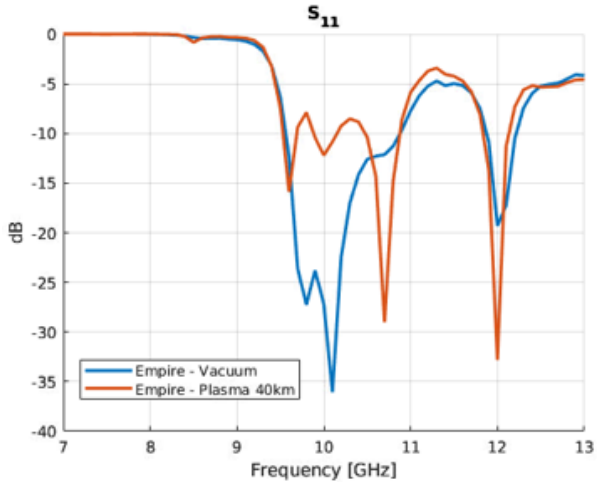

(a) Reflection coefficient.

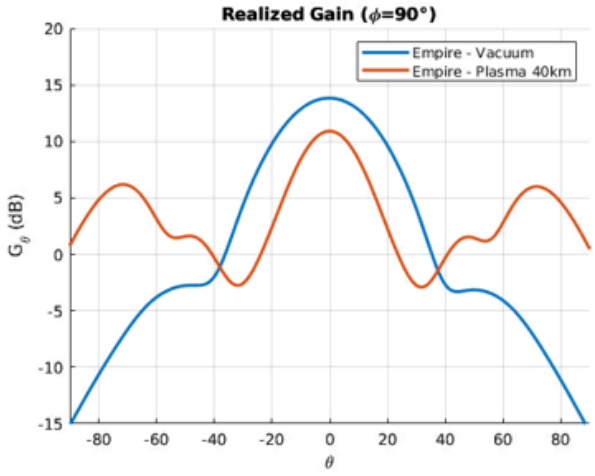

(b) Realized gain for 90 degrees, with and without a re-entry plasma.

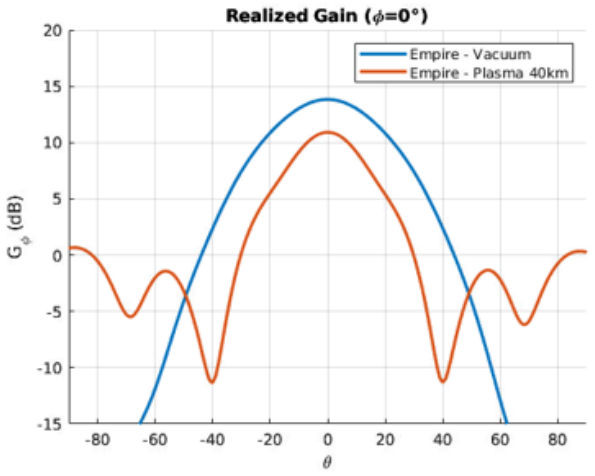

(c) Realized gain for 0 degrees, with and without a re-entry plasma.

Figure 3-2. Computed effect of the re-entry plasma on the RAM-C2 aft X-band horn antenna. Performance under vacuum conditions and for conditions resembling re-entry at 40 km, where a laminar plasma layer is present, are shown. The peak plasma frequency at 40 km is 9 GHz.

S_{11} is significantly altered by the plasma. Notice that the resonance at $\sim$ 10 GHz is shifted up by several hundred megahertz.

Additionally, the far field radiation pattern is also affected by the re-entry plasma. We used the Empire frequency domain NTFF to compute the far field patterns for the vacuum and 40 km plasma cases. The results, for both polarizations, are shown in Fig. 3-2 (b) and (c). The plasma attenuates the 10 GHz far fields by nearly 3 dB and causes significant narrowing of the main lobe. The enhanced side lobes are an artifact of the far field calculation due to choice of Huygens surface.

This page intentionally left blank.

4. MICROWAVE SIGNAL FLUCTUATIONS DUE TO A TURBULENT RE-ENTRY BOUNDARY LAYER

In general, re-entry plasmas cause attenuation and scattering of microwave signals. It stands to reason that efforts to model microwave interactions with re-entry plasmas can benefit by drawing from the well established field [23] of microwave signal propagation in attenuating and scattering media. It's useful to distinguish between two classes of problems: scattering problems and line-of-sight problems, sketched in Fig. 4. Line of sight problems are concerned with the line-of-sight propagation between a transmitter and receiver. Scattering problems are concerned with the reception of some scattered signal.

Let's look at the line-of-sight propagation from a hypothetical RAM-C2 antenna to a distant receiver, perhaps a ground station. At 28 km altitude, RAM-C2 was at the deepest point of radio blackout and the boundary layer is believed to have been turbulent. A detailed analysis of this problem can be found in [14] and we give a brief account of the main results here. Note that in this line-of-sight problem, we are essentially studying the properties of the electric far field, underscoring the importance of an accurate near to far field transformation of the raw Empire solution.

The model is a rectangular aperture antenna which terminates on an infinite ground plane. In the Empire electromagnetic simulations, the antenna is driven by a sine-modulated Gaussian pulse signal with a wide spectrum between approximately 15 and 30 GHz. The plasma layer model has a randomly fluctuating electron density which is prescribed according to an approach analogous to that used by Trolinger and Rose [24], which has been used to estimate optical performance in hypersonic environments.

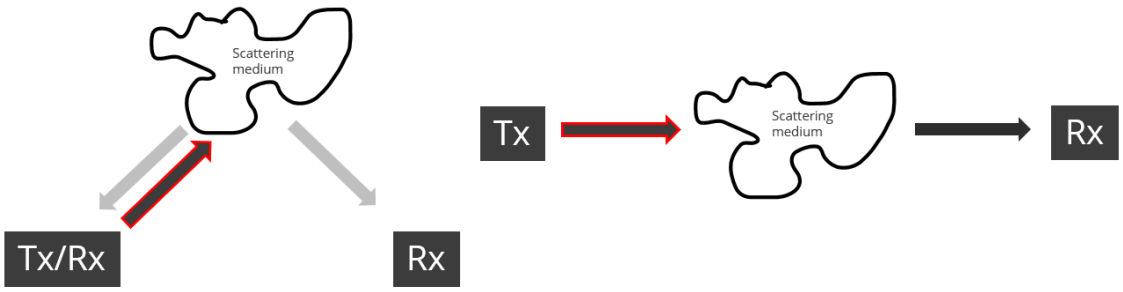

(a) Scattering problem **(b) Line-of-sight problem**

Figure 4-1. The two basic classes of problems for microwave propagation through random media.

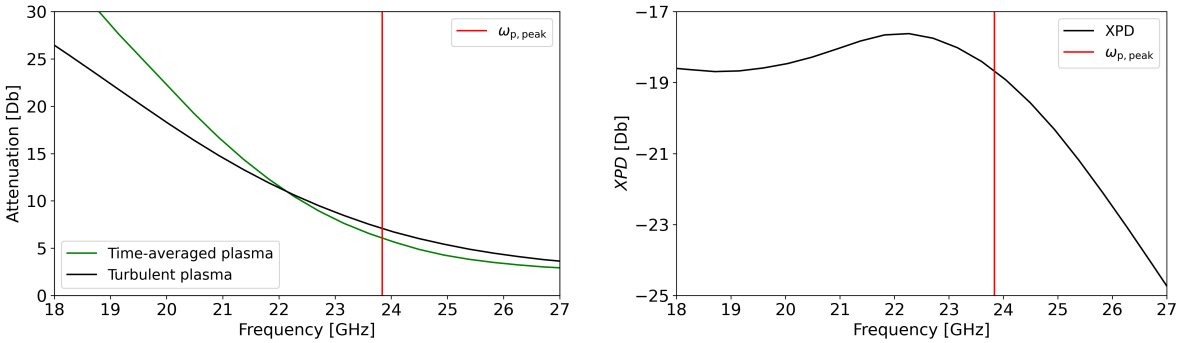

(a) Attenuation **(b) Depolarization**

Figure 4-2. Attenuation and depolarization (XPD) of the signal which has been transmitted through a turbulent re-entry boundary layer model.

4.1. Transmitted signal attenuation

A concise and detailed quantitative characterization of the transmitted signal is indeed possible. First, consider the attenuation due to the re-entry plasma. Signal attenuation at the receiver for the turbulent plasma layer model and for a time-averaged plasma model are shown in Fig. 4.2 (a). Attenuation for the turbulent plasma model was computed by averaging over an ensemble of thousands of random plasma fluctuation states.

At higher frequencies the time-averaged plasma layer is less attenuating, on average, than the fluctuating plasma fields. Then there is a cross over at around 22 GHz. Below the cross-over frequency, the time-averaged plasma is more attenuating. Below 22 GHz, the signal is in "deep blackout" and occasional windows of good transmission open up, leading to an increase in average transmitted power. Above the cross over, scattering attenuation is significant compared to plasma absorption.

4.2. Transmitted signal depolarization

Take a look at the polarization of the signal, shown in Fig. 4.2 (b). Under vacuum conditions or if the plasma is laminar, the antenna transmits a linearly polarized signal. However, with a turbulent re-entry plasma, the signal is partially depolarized. The strength of depolarization can be quantified with the cross-polarization discriminate (XPD),

$$XPD(\omega) = 10\log\left(\frac{\langle|\mathscr{E}_{x,i}|^2\rangle}{\langle|\mathscr{E}_{y,i}|^2\rangle}\right), \tag{4.1}$$

where $\mathscr{E}_{x,i}$ and $\mathscr{E}_{y,i}$ are the transverse components of the frequency-domain electric far field.[1]

With the model based on the Trolinger and Rose model, the plasma electron density fluctuations are isotropic. The fluctuations are a superposition of spherical perturbations. We'll see in section 5 that

[1]This definition assumes that the far field signal is nominally polarized in the y-direction

the depolarization due to a realistic (large eddy simulation model) plasma layer, with anisotropic electron density fluctuations, causes a much stronger depolarization — by about an order of magnitude.

4.3. Transmitted signal first order statistics

Next we attempt to characterize the co-polarized amplitude and phase fluctuations at the receiver. In the established theory of electromagnetic scattering from random media [23] and also the theoretical study of turbulence [25], the task of characterizing fluctuations is approached through the lens of random functions.

Uncorrelated fluctuations, or *white noise*, can be described by a probability density function (PDF) of a single random variable. The description of correlated fluctuations (*colored noise*) requires a joint PDF of multiple random variables. In general, a random function requires an infinite dimensional joint PDF although this is not practical. One can obtain an n^{th} order joint PDF describing a random function from its $n+1^{th}$ order description; the description of a random function can be "closed" at some "order" for an approximate description. This closely parallels the use of fluid models in approximating Boltzmann kinetic systems, where a fluid model is associated with some number of moments (density, velocity, pressure, etc.) and the system's dependence on higher moments is approximated in its closure [26].

It is standard practice to use a second order description, particularly a Gaussian process description because they are easy to work with. A Gaussian process [27] is completely described by its covariance function or equivalently (for stationary processes) its power spectral density (PSD). We will take this approach.

First, however, we will consider the first order statistics of the amplitude and phase fluctuations. That is, we will consider their univariate PDFs. Estimates of the amplitude fluctuation PDFs for several microwave frequencies are given in Fig. 4.3. The fluctuations have lognormal fading below approximately 22 GHz. Between roughly 22 GHz and the peak plasma frequency, 23.7 GHz, there is a transition from lognormal to Rice amplitude fading. As the frequency increases from approximately 23.7 GHz, the Rice shape parameter K increases from zero. This represents a transition from Rayleigh fading to Gaussian fading. The Wang-Strohbehn distribution [28] is effective at modeling the amplitude fading at all microwave frequencies. The Wang-Strohbehn distribution is a product distribution of a Rice distributed random variable with a lognormally distributed random variable.

A strong physical intuition regarding the channel properties emerges, if we relate these observations of the amplitude fading to the well known [29] physical interpretation of lognormal fading and Rice fading. Lognormal fading arises from multiple scattering along a narrow path of propagation, while Rice fading occurs when there is a much wider path of propagation which leads to many uncorrelated single scattering events contributing to the transmitted signal. Recall, in Fig. 3-2, that narrowing of the main lobe is observed in connection with attenuation by a re-entry plasma layer, so intuitively we can expect this transition from Rice to lognormal statistics as the frequency decreases below the plasma frequency. At more strongly attenuated frequencies, the path of propagation is

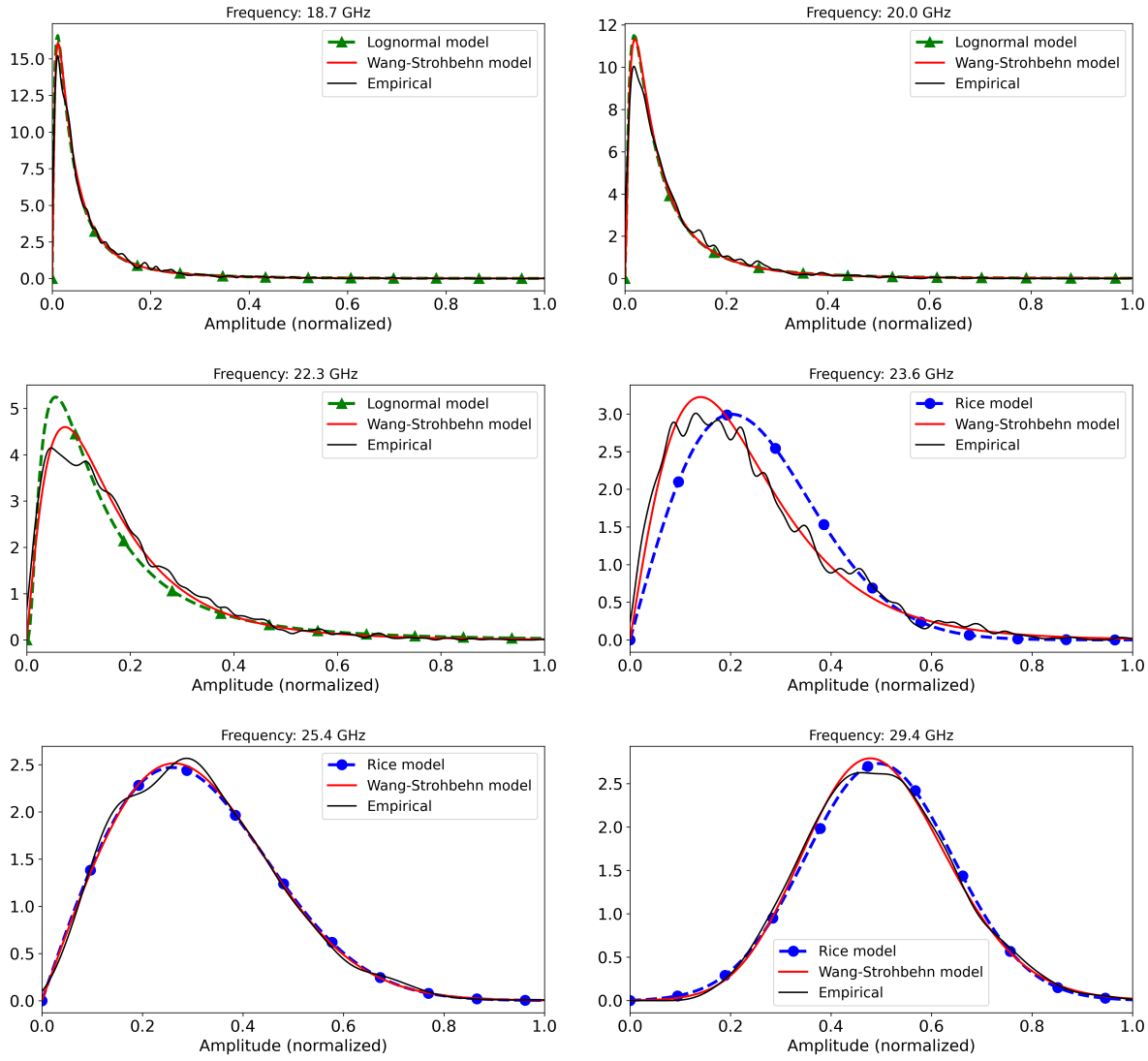

Figure 4-3. First order statistics of the amplitude fluctuations. In each plot, either the Rice or lognormal fit is shown, depending on which model has a higher likelihood for the data. The Wang-Strohbehn distribution fits the data at all frequencies considered.

narrower. The Wang-Strohbehn distribution is essentially a model that allows for a continuously variable cone of propagation, recovering the lognormal and Rice distributions in the limits of narrow cone and wide cone propagation through the scattering medium.

This interpretation of the fading statistics sets an expectation that a 1D simulation would never recover a Rice amplitude fading, although we did not verify this by calculation. Indeed, the first study to attempt a characterization of the signal fading for re-entry environments [30] used 1D simulations and found lognormal amplitude fluctuations.

4.4. Transmitted signal second order statistics

Now consider a second order statistical description of the amplitude and phase fluctuations: a Gaussian process model. We recognize that, any time the univariate PDF of a random function is not a Gaussian, the function cannot be exactly described by a Gaussian process. And, in this context, the amplitude fluctuations are mostly not Gaussian as we saw in Section 4.3. In practice, however, this is often done as an approximation. As we pointed out in [14], it could be worthwhile to explore better descriptions than the Gaussian process in future work.

We observed a strong anti-correlation between amplitude and phase at all microwave frequencies. Thus information about the fluctuation in one quantity gives us information about the other. Modeling the fluctuations in amplitude and phase with a standard, single-output Gaussian process (SOGP) misses an opportunity to account for this correlation. Therefore, we suggest using a multi-output Gaussian process model. In the following, it is shown that an MOGP is highly effective for modeling the amplitude and phase fluctuations due to plasma turbulence.

At a given microwave frequency, the auto and cross covariance functions for the amplitude and phase fluctuations can be estimated,

$$\hat{B}_{ij}(\tau_k \; ; \; \omega) = \frac{w(\tau_k)}{N - |k|} \sum_{l=1}^{N} \big(q_i(t_{l+k}) - \langle q_i \rangle\big)\big(q_j(t_l) - \langle q_j \rangle\big), \tag{4.2}$$

from the amplitude samples q_1 and phase samples q_2. The lag time, $\tau_k = k\Delta T$. The window function w is selected for improved estimates at large lags.

The covariance functions $\hat{B}_{ij}$ can inform a multi-output Gaussian process (MOGP) model for the phase and amplitude [31]. We demonstrate the efficacy of the MOGP model by reconstructing the phase from measurements of the amplitude along with occasional measurements of phase, shown in Fig. 4-4.

The MOGP provides an extremely compressed and accurate reduced order model (ROM) for the amplitude and phase fluctuations. To communicate a precise description of fluctuations in the transmitted amplitude and phase of a re-entering object, one needs only the cross-covariance functions for those quantities. A more detailed discussion can be found in [14].

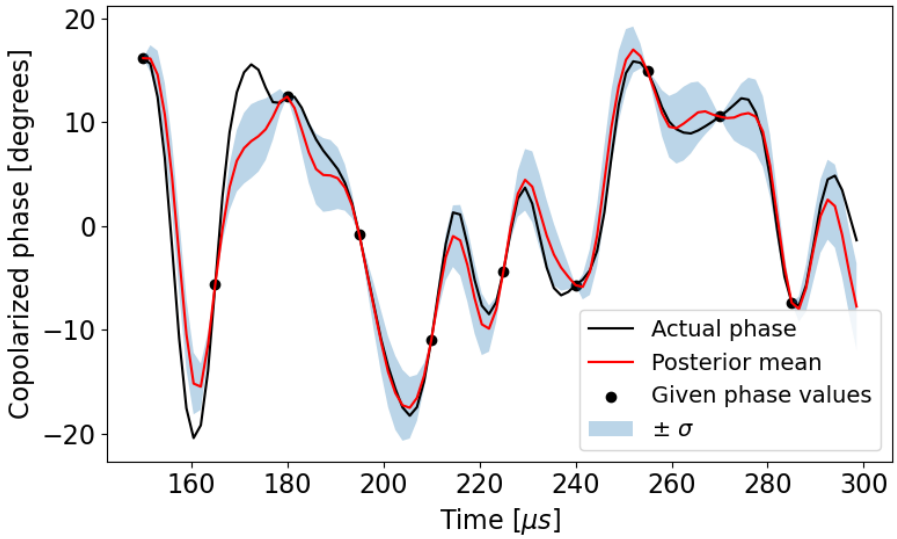

Figure 4-4. The transmitted signal phase is reconstructed from occasional phase measurements (indicated by the circle markers) and full knowledge of the amplitude (not plotted).

5. INTERPRETATION OF THE LOW ALTITUDE RAM-C2 REFLECTOMETER MEASUREMENTS

In the RAM-C2 experiment, emphasis was on collecting data concerning antenna performance characteristics and plasma profile information at high altitudes. The Langmuir probes, used to measure the plasma profile within the aft flow field, provided accurate data down to around 73 km, with accuracy at lower altitudes compromised due to extreme heating or loss of signal [8, 7]. The reflectometry data was interpreted according to the *slope technique*, whereby a sharp rise in reflection coefficient was taken to correspond to the peak plasma frequency reaching the O-wave cutoff. This technique was not expected to work at low altitudes, due to the high electron collision frequency. A high electron collision frequency softens the jump in reflection coefficient in the neighborhood of the cutoff frequency. This is evident by inspection of Fig. 1-1.

Yet the reflectometers provided interesting observations at low altitudes. The four X-band reflectometers saw a sudden drop in their reflection coefficients S_{11}. However, these events are believed not to have coincided with a drop in plasma electron density [6]. Rather, these events have been connected to a transition to boundary layer turbulence, and it was proposed that reflectometry data could be used as an instrument to detect the onset of turbulence in the boundary layer [7].

The connection to boundary layer transition follows from the observation that the S_{11} drops occurred in a sequence that corresponds to the distance from the nose tip; the aft-most reflectometer was the first to record a sudden drop in S_{11} and the forward-most was last. In their figure, Huber, Schexnayder and Evans [7, 6] indicated that the moments of low-altitude S_{11} transition correspond well to the acheivement of a local Reynolds number 3.5×10^5. They suggested that the S_{11} decay may occur at the moment of transition due to the change in plasma profile shape.

We have used the newly developed capabilities in Empire and SPARC to gain further insight and to validate Schexnayder's hypothesis, that the S_{11} decay may occur at the moment of transition due to the change in plasma profile shape. The following provides a summary and a detailed account is given in [32].

We considered a hypothetical rectangular aperture antenna, with a 15 GHz cutoff frequency, mounted on the conical RAM-C flight body. The antenna is located three nose diameters aft of the nosecone tip. The antenna was rung with a sine-modulated Gaussian pulse in the K to Ka frequency bands.

We considered several models for the plasma layer, all of which were computed with SPARC [5]. A non-equilibrium, 11-species reacting flow model, based on the Park model [33], was used to obtain electron densities. The flow was assumed to be free of any impurities in these models. The flight conditions correspond to those of RAM-C2 at 28 km altitude.

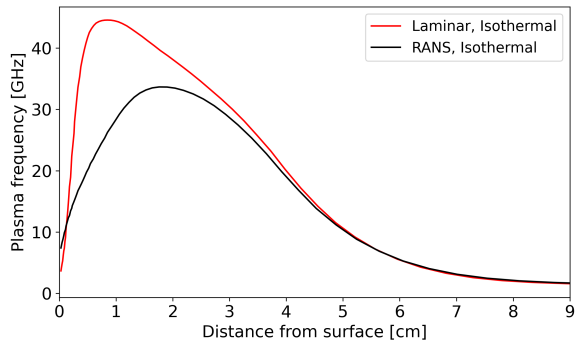

(a) Plasma layer models using the isothermal wall boundary condition. The RANS model plasma layer differs substantially from the laminar, non-turbulent model. In particular, the plasma is shifted further from the vehicle body with the RANS model.

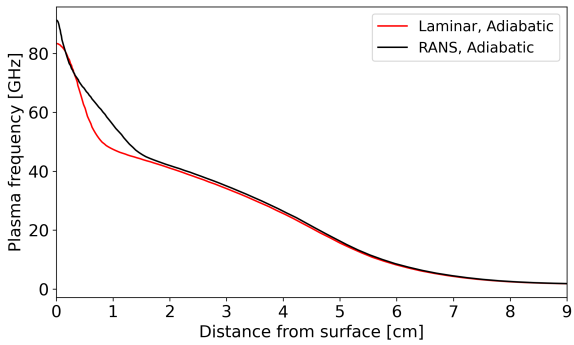

(b) Plasma layer models using the adiabatic wall boundary condition. The plasma densities are much higher than for the isothermal wall model.

Figure 5-1. The steady flow plasma profiles at the antenna location.

5.1. Steady flow plasma layer models

First, we consider steady flow, non-fluctuating plasma layer models. We computed the antenna response for four models. Two models assume laminar, non-turbulent flow, while the other two models used a two-equation Reynolds–averaged Navier-Stokes (RANS) model for the turbulence closure. Two boundary conditions were considered: an isothermal wall with T=293 K and an adiabatic wall. The four plasma profiles are shown in Fig. 5-1.

The result for the adiabatic wall plasma models is trivial and not unexpected: the signal is almost entirely reflected, $S_{11} \approx 0$ dB. However, a much more interesting story can be told regarding the isothermal wall plasma layer models. The reflection coefficients for these plasma layers, and for the no-plasma vacuum case, are plotted in Fig. 5-2. At low frequencies, under 23 GHz, S_{11} is similar for both plasma profiles. However, as the frequency increases above 23 GHz, S_{11} for the RANS profile quickly transitions to approximate the vacuum, no-plasma value.

Within a certain frequency range, then, our calculations indicate a drastically lower reflection coefficient S_{11} for a turbulent plasma compared to a laminar plasma. But this is what was observed experimentally for RAM-C2.

A clear picture emerges if we look at the frequency domain, 29 GHz electric field, shown in Fig. 5-3. The 29 GHz field is considered because this is the frequency for which there is the greatest difference in S_{11} between the laminar and turbulent plasma models. The turbulent plasma layer supports a surface wave at this frequency and the laminar plasma model does not. When the plasma layer is turbulent, most of the signal energy converts to the surface mode and propagates away from the antenna. For the laminar plasma layer, most of the signal is reflected back into the antenna aperture.

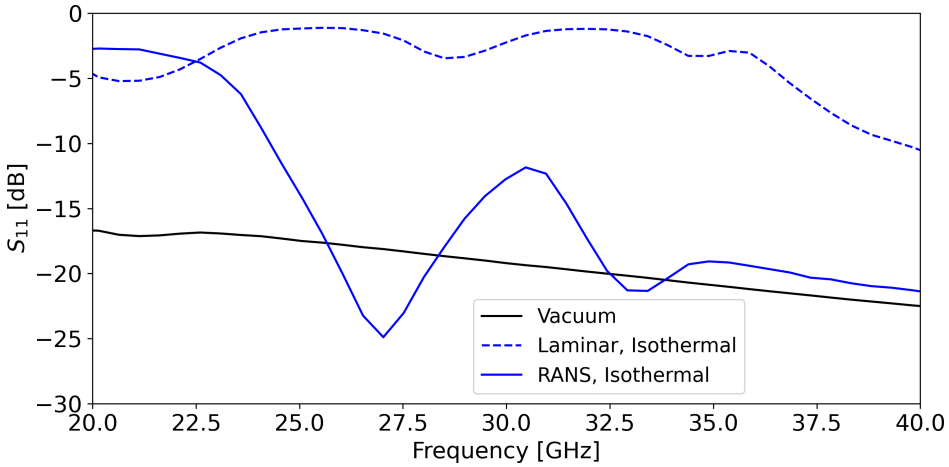

Figure 5-2. Computed reflection coefficients for the steady flow, isothermal boundary plasma layer models, as well as the vacuum case for which there is no plasma.

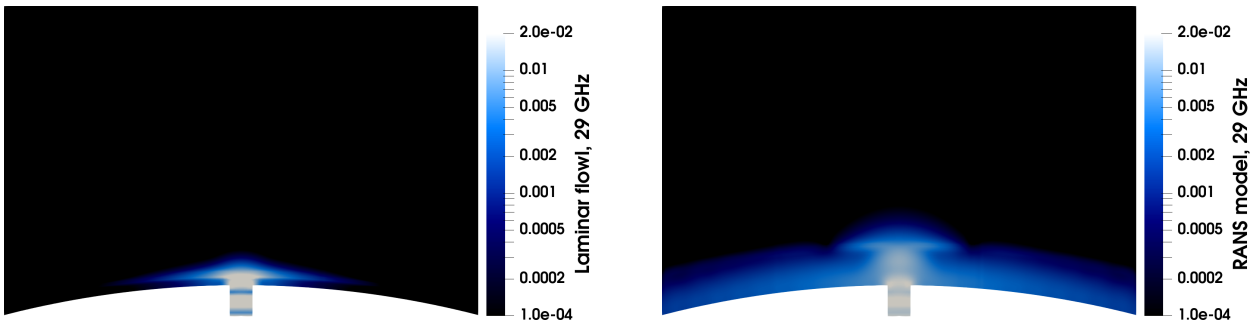

(a) Laminar plasma layer model

(b) RANS plasma layer model

Figure 5-3. Frequency domain electric field, for 29 GHz, for the laminar and RANS plasma profiles. For the turbulent RANS plasma, a surface mode is excited. The surface mode allows energy to flow away from the antenna aperture. For the laminar, non-turbulent plasma, there is no significant surface mode behavior and most of the energy is reflected back into the antenna aperture.

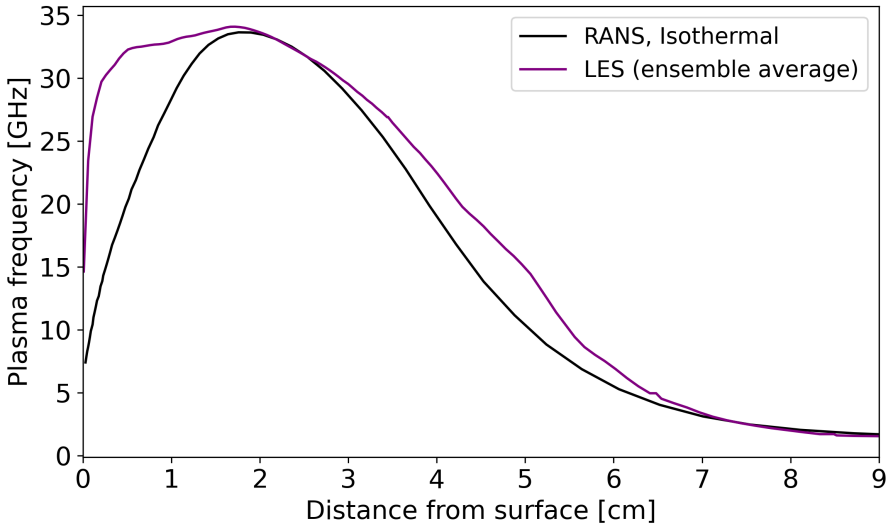

Figure 5-4. Comparison of the RANS, isothermal plasma profile with the ensemble averaged plasma profile for the LES model.

The reflection coefficient S_{11} is substantially diminished for frequencies that exhibit robust surface mode propagation. This is observed when the plasma standoff distance is greater than approximately half a wavelength. We conclude that a sharp drop in reflection coefficient can be observed when the boundary layer transitions to turbulence, if the plasma standoff distance suddenly increases due to transition. This sudden increase in plasma standoff distance, when the boundary layer transitions, is predicted by the present series of simulations.

5.2. Fluctuating flow plasma layer model

We obtained a time-fluctuating model of the plasma layer from a SPARC large eddy simulation (LES) of the flow around RAM-C2 at 28 km altitude. The details of the LES setup are given in [32]. In aggregating the following statistics, we considered 100 frames, spaced $\Delta t = 1$ μs apart. Contrary to the results of section 5.1, it can be seen in Fig. 5-4 that, on average, plasma is shifted inwards from the steady-state RANS result. The plasma standoff distances are therefore smaller than for the RANS case. The exact cause of this difference between the steady-state model's profile and the profile resulting from averaging the time-varying model's profiles is still unknown and further investigation is warranted. As a result of the near-wall difference, we observed reflection coefficients, S_{11}, which were, on average, much higher than the vacuum or RANS S_{11} values even for frequencies above 23 GHz.

Next, we consider the line-of-sight transmission properties of the LES plasma model, shown in Fig. 5-5. It is not surprising that the ensemble-averaged attenuation for the LES plasma layer model is substantially higher than for the RANS, isothermal model; the LES model averaged electron density profile is thicker and with a slightly larger peak density. Note that the cross-polarization (XPD) is significantly stronger for this model compared to the surrogate model considered in section

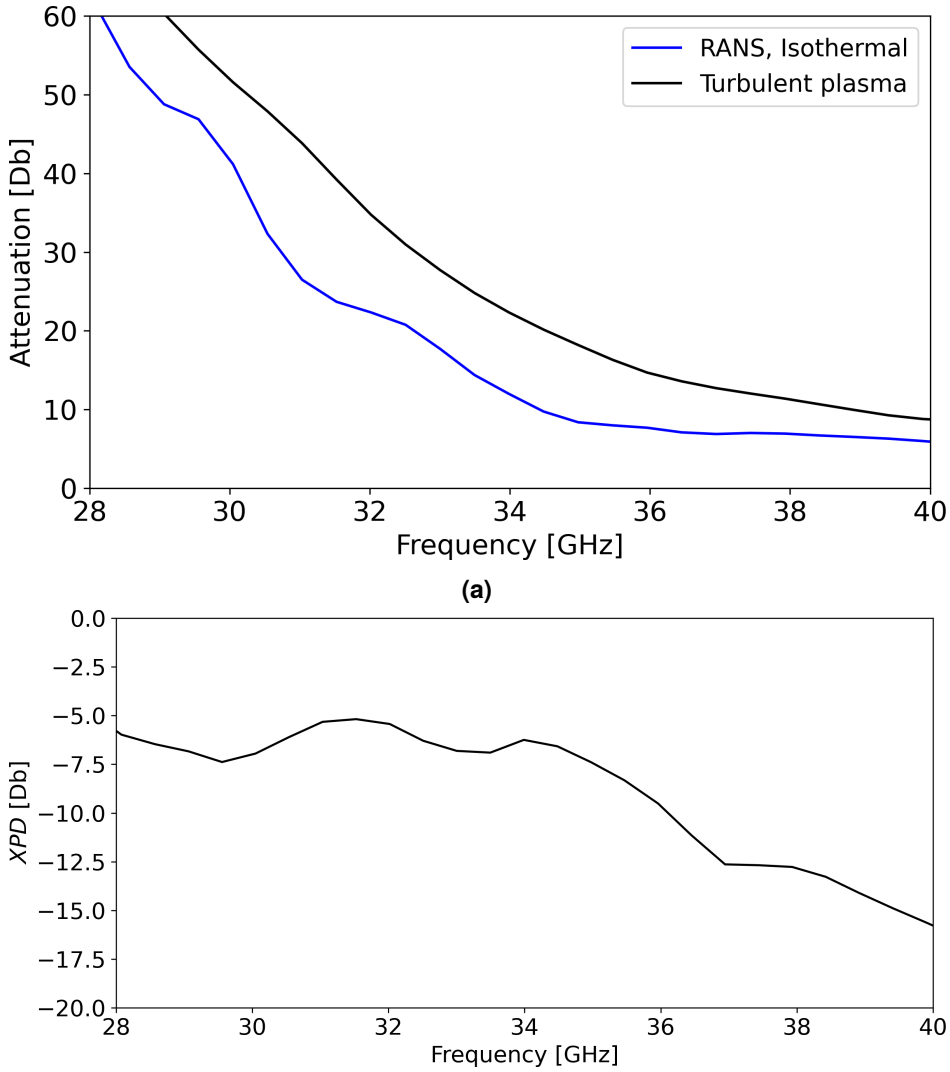

Figure 5-5. Attenuation and depolarization (XPD) for the LES plasma model. Both of these quantities were obtained by an ensemble average over all 100 frames.

4. This may be due to the anisotropic nature of the electron density fluctuations in the LES model. In the Trolinger-and-Rose-inspired model, the density fluctuations are a superposition of spherical perturbations hence there is no preferred direction (the density fluctuations are isotropic).

This page intentionally left blank.

6. PLASMA PROFILE RECONSTRUCTION FROM MICROWAVE MEASUREMENTS

A number of diagnostic techniques can be used to infer information about the re-entry plasma profile. RAM-C2 employed Langmuir probes, which are placed in the plasma to measure plasma density and temperature. They produce signals, resulting from the plasma sheath response, that can be interpreted to provide this information. But Langmuir probes present some serious drawbacks. They will perturb both the plasma and the aerodynamic flow; it is an invasive measurement technique. In the RAM-C2 experiment the probe measurements were valid only down to a certain altitude due to heating of the probes. Optical techniques are compelling for measuring entry plasma properties. For example, UV/visible spectroscopy is a popular approach [34]. The lengthier review [35] discusses a number of approaches including invasive probes (including Langmuir probes) and laser diagnostics (Thompson scattering, laser induced fluorescence, etc.) for diagnosing ionized, hypersonic flows.

The RAM-C2 experiments were also equipped with reflectometers positioned along the vehicle axis. They inferred the plasma density with the *slope technique*. At the moment a sharp rise in reflection coefficient is detected, the peak plasma density at that sensor location is assumed to be equal to the critical plasma density, $\omega = \omega_{\mathrm{p}}$. They also used the phase of S_{11} to infer the plasma standoff distance. In their model [8], the reflected phase is,

$$\theta = \theta_d + \theta_r \tag{6.1}$$

$$\theta_d = 2\pi \frac{2d}{\lambda_0} \tag{6.2}$$

$$\theta_r = \pi, \tag{6.3}$$

where the phase change due to reflection off the critical density contour in the plasma is θ_r and the phase change due to propagation through the plasma is θ_d and λ_0 is the free space wavelength of the probing signal.

There are a few issues with this early reflectometry technique. The model for the reflected phase change θ does not take into account the effect of the plasma on the probing signal wavelength. Also the slope technique is not reliable at low altitudes. The increase in electron collision frequency at low altitudes smooths the transition at the cutoff frequency, as shown in Fig. 1-1. Furthermore, as noted in section 5, sharp changes in S_{11}, unrelated to changes in the peak plasma density, were observed at low altitudes.

In the 1980s and beyond, significant advancements in reflectometry as a plasma diagnostic were made by the magnetic confinement fusion plasma community. In that application, the plasma is strongly magnetized and X-mode reflectometry is often preferred [36]. However, in the re-entry problem the plasma is unmagnetized and we must use O-mode reflectometry.

Inversion of the O-mode reflected phase, to obtain the plasma profile, can be achieved [37] by an inverse Abel transform,

$$x_c(\omega_p) = x_0 + \frac{c}{\pi}\int_{\omega_{p,0}}^{\omega_p} \frac{d\omega}{\sqrt{\omega_p^2 - \omega^2}} \frac{d\phi\,(\omega)}{d\omega}, \tag{6.4}$$

where $x_c(\omega_p)$ and x_0 are the cutoff positions associated with frequencies ω_p and $\omega_{p,0}$, respectively.

In general, O-mode reflectometry can only be expected to provide information about the plasma profile over the interval for which the plasma density increases monotonically with distance from the reflectometer. This is a serious issue for re-entry plasmas. A commonly used parameterization for re-entry plasmas is the bigaussian profile, which exhibits a monotonically increasing inboard side, a peak and then a monotonically decreasing outboard side. Another drawback of the Abel inversion is that it requires many frequency bands (one for each electron density contour).

We will explore techniques for plasma profile reconstruction which are better suited for re-entry plasmas than the Abel transform. Sections 6.1, 6.2, 6.3 and 6.4 are concerned with 1D reflectometry methods. The 1D transmission matrix model for inhomogeneous plasma slabs is introduced in Section 6.1. Then the validity of the WKB approximation to estimate reflected phase for re-entry plasmas is explored in Section 6.2. In section 6.3, a reconstruction technique, based on the WKB approximation within a 1D inhomogeneous plasma slab, is developed. The technique is similar to the Abel transform but accounts for additional dispersive effects.

In section 6.5, we'll show that re-entry plasma profiles can be reliably reconstructed from dual-band reflectometer measurements. We will show that O-mode reflectometry can gather significant information about the outboard side of the plasma profile. When the spatial dimensions of the plasma are small or comparable to the probing signal wavelength, evanescent wave activity returns information about the outboard side of the profile to the reflectometer aperture. Also, the ambient air pressure during re-entry plasma formation is typically much higher than the pressure in a tokamak. The significant electron collision frequency ν in re-entry plasmas, due to high air pressure, allows O-mode propagation past the cutoff $\omega = \omega_{\mathrm{p}}$.

6.1. One-dimensional Planar Inhomogeneity

Re-entry plasmas typically have a rapidly varying electron density profile normal to the vehicle surface, often approximated by a bigaussian function [13]. The density varies slower along the direction of the flow and can often be locally well represented as a planarly layered media with one-dimensional inhomogeneity. For this situation, the electromagnetic vector wave equations simplify to two scalar wave equations, one for the transverse electric (TE) and one for the transverse magnetic (TM) waves in the media [38]. If the electron densities and resulting permittivities vary continuously, these wave equations can be solved using various numerical methods. However, if the continuously varying profile is modeled as piecewise constant functions, then an analytical solution can be written for each region and a unique solution found by matching the boundary conditions at the discontinuities. A plane wave solution results. Applying this approach results in an analytical

solution for the reflection and transmission coefficients of the finely discretized multilayered plasma. For TE waves, the recursive relation for the generalized reflection and transmission coefficients for a z-oriented inhomogeneity are

$$\tilde{R}_{i,i+1} = \frac{R_{i,i+1} + \tilde{R}_{i+1,i+2} e^{2ik_{i+1,z}(d_{i+1}-d_i)}}{1 + R_{i,i+1}\tilde{R}_{i+1,i+2} e^{2ik_{i+1,z}(d_{i+1}-d_i)}} \tag{6.5}$$

and

$$\tilde{T}_{1,N} = \prod_{j=1}^{N-1} e^{ik_{j,z}(d_j - d_{j-1})} S_{j,j+1} \tag{6.6}$$

with

$$S_{i-1,i} = \frac{T_{i-1,i}}{1 - R_{i,i-1}\tilde{R}_{i,i+1} e^{2ik_{i,z}(d_i - d_{i-1})}}, \tag{6.7}$$

respectively. Where $\tilde{R}$ and $\tilde{T}$ are the generalized reflection and transmission coefficients, R and T are the reflection and transmission coefficients for a single interface, k is the propagation constant, and d is the layer interface position.

Compared to full-wave electromagnetic approaches, the analytical solution is valuable since it can be calculated quickly allowing for large numbers of plasma profile scenarios and frequencies to be evaluated rapidly. This is particularly useful for optimization where large numbers of iterations are often needed to achieve an optimized solution. The analytical approach provides intuition and a good initial solution that can later be refined using more computationally expensive full-wave simulation methods.

6.2. Reflectometry Solution Comparison: Exact and WKB Approximated Reflection Coefficient Phases

Reflectometry methods often assume the plasma profile's electron density is monotonically increasing away from the reflectometer. This is a necessary assumption since waves reflecting at a cutoff layer do not penetrate further into the profile, so the layers beyond are obscured. Reflectometry methods also typically assume the WKB (Wentzel, Kramers, and Brillouin) approximation, which is a high-frequency method that ignores the higher-order multiple reflections of the wave within the stackup [38]. The WKB approximation is technically invalid where critical reflections occur, but can still be used with good results in certain laboratory plasma reflectometry cases [37]. Since the Abel transform reflectometry formulation relies on critical reflections within the plasma profile and assumes the WKB approximation, understanding the validity of the WKB assumptions for reentry plasma density and frequency regimes is valuable. To do so we consider a simplified, contrived plasma profile with linearly increasing electron density from $N_{e,1GHz} = 1.2407 \times 10^{10}/cm^3$ to $N_{e,9GHz} = 1.0049 \times 10^{12}/cm^3$ (plasma frequency from 1 to 9 GHz) over an 8cm span defined by

$$N_\mathrm{e} = \frac{N_\mathrm{e,9GHz} - N_\mathrm{e,1GHz}}{8\ \mathrm{cm}} z + N_\mathrm{e,1GHz} \tag{6.8}$$

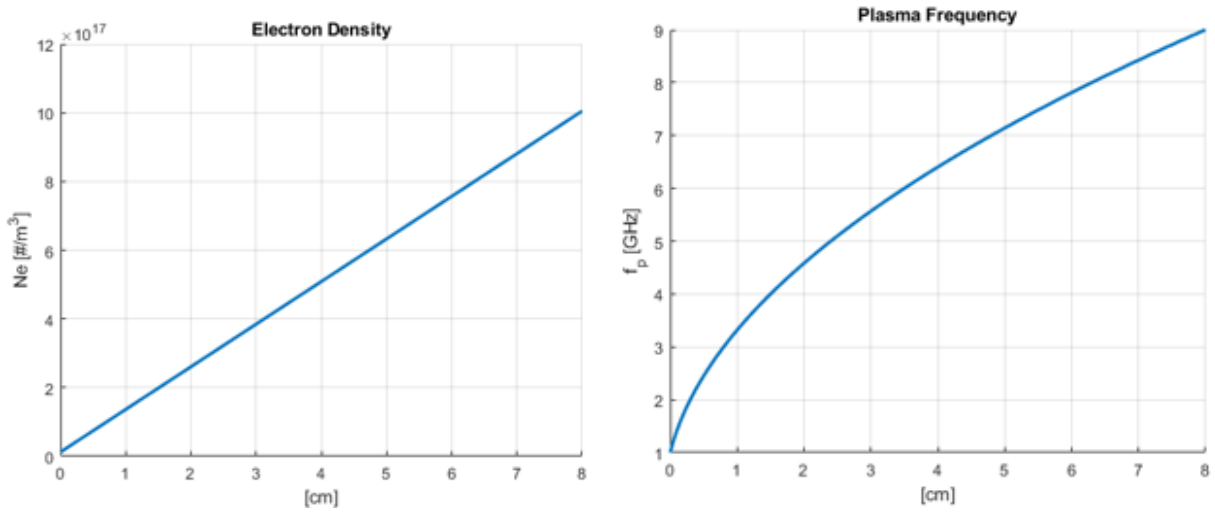

Figure 6-1. Example linear electron density profile and associated plasma frequency.

with

$$\omega_p^2 = \frac{N_e q_e^2}{m_e \varepsilon_o}. \tag{6.9}$$

q_e is the electron charge, m_e is the electron mass, ε_o is the premittivity of free space, and z is the position in the profile. The resulting profile electron density and plasma frequency are illustrated in Fig. 6-1.

The reflection coefficient phase for the profile is found at frequencies from 1 to 9 GHz. The phase is first found using Eqn. 6.5, which is the exact solution. The phase is indicative of the propagation delay of the signal within the profile and the reflecting boundary conditions. The reflection coefficient phase is then found using the WKB approximation, which ignores higher order reflections in the stackup. The reflection coefficient phase using the WKB approximation is

$$\phi(\omega) = 2\int_{z_o}^{z_c(\omega)} k(\omega, z)\, dz - \frac{\pi}{2} \tag{6.10}$$

where k is the propagation constant varying throughout the stackup, z_o is the position of the start of the profile, and $z_c(\omega)$ is the point of cutoff and complete reflection within the profile for frequency ω. Perfect reflection at the first overdense cutoff layer ($\omega_p = \omega$) is also assumed for this WKB solution case.

The reconstructed profiles based on the exact reflection coefficient phase solution and the WKB approximated phase solution compared to the truth solution are shown in Fig. 6-2. The standard Abel transform reconstruction approach is fundamentally based on the WKB approximation in its formulation. Therefore, we expect the reconstructed profile to match closer to the truth when the algorithm is given reflection coefficient phases also calculated using the WKB approximation. This is seen in the results. On the other hand, the reconstruction based on the exact phase solution is affected by imperfect wave reflection and higher order reflections in the reflection coefficient phase solution. These are unaccounted for in the fundamental reconstruction formulation. These unaccounted-for effects lead to error in the reconstructed profile, but are representative of what a

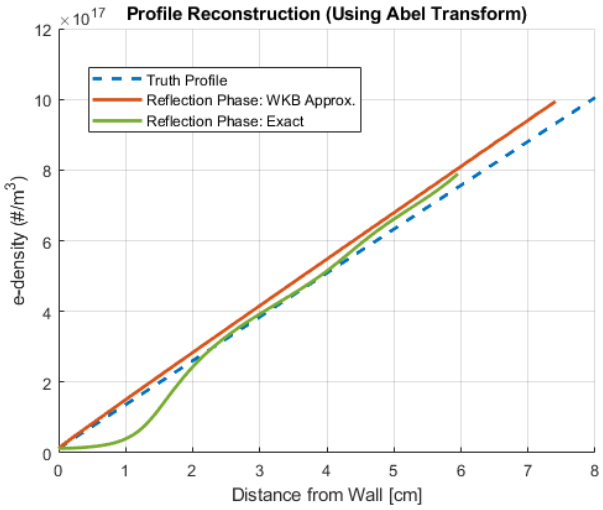

Figure 6-2. Comparison of the Abel transform profile reconstruction determined from the reflected phase calculated from the exact and the WKB approximated reflection coefficient solutions. Realistic reflectometer performance is represented by the exact calculated reflection phase solution.

reflectometer would measure in practice. This shows a potential limitation of the Abel transform based reflectometry approach for the reentry problem. Futhermore, the lower electron density layers near the base of the profile are ultimately reconstructed by the lower frequency signal content, since higher frequency waves pass through these layers relatively unaffected. Since the WKB-based reconstruction approach is ultimately a high frequency approach, the results are less accurate at these lower frequencies. The accuracy of the reflectometry method will ultimately be situation dependent. Reentry plasmas are also collisional, which means they do not have perfect reflection at the collisionless cutoff layer.

6.3. New Profile Reconstruction Formulation

As seen in Fig. 6-2, the Abel transform based reflectometry implementation has a discrepancy between the truth profile even when the WKB approximation is used in the generation of the underlying phase data. To understand this discrepancy better, we pursue a new, intuitive derivation of a reconstruction algorithm based strictly on the WKB approximation. The propagation paths producing the reflection phases for different frequencies based on the WKB approximation are illustrated in Fig. 6-3.

The lowest frequency wave ω_0 reflects off the initial profile layer producing a round trip phase of ϕ_0. The next incremental frequency higher ω_1 propagates through the initial layer with plasma frequency $\omega_{p,0}$ since the frequency is slightly higher than the cutoff frequency and reflects off the next layer with plasma frequency $\omega_{p,1}$. We can write the position of the $\omega_{p,1}$ layer as

$$x_1(\omega_{p,1}) = x_0(\omega_{p,0}) + \frac{\phi_1 - \phi_0}{\omega_1 - \omega_0}\frac{1}{k_{p,0}}\Delta\omega \tag{6.11}$$

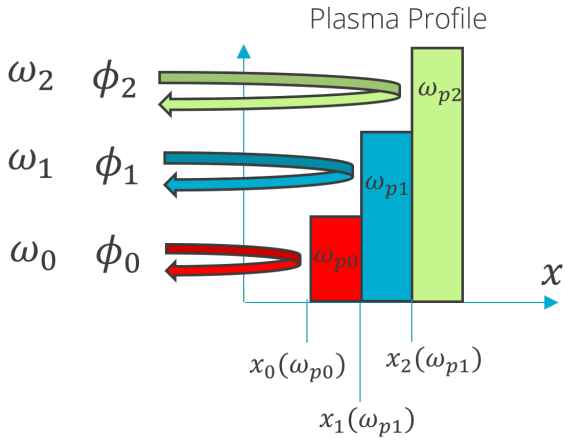

Figure 6-3. Propagation phases based on the WKB approximation for a monotonically increasing electron density profile.

where ϕ_0 and ϕ_1 are the round-trip propagation phases for frequencies ω_0 and ω_1, respectively. $\Delta\omega$ is the frequency increment $\Delta\omega = \omega_1 - \omega_0$ and $k_{p,0}$ is the propagation constant of the initial layer given generally for frequency ω as

$$k = \frac{\omega}{c}\sqrt{\varepsilon_r} = \frac{\omega}{c}\sqrt{1 - \frac{\omega_p^2}{\omega^2}} = \frac{1}{c}\sqrt{\omega^2 - \omega_p^2} \tag{6.12}$$

where ε_r is the relative permittivity.

This expression intuitively relates the measured phase change over an incremental frequency to the position of a plasma frequency layer. As the frequency continues to increase to reconstruct the remaining profile, the dispersive nature of the plasma must be accounted for. Each frequency will propagate through the layers with different phase delays, so the phase contributed by the layer between interfaces N-1 and N is

$$\phi_N - \phi_{N-1} = \frac{\sqrt{\omega_N^2 - \omega_p^2}}{c} l_N + \sum_{n=1}^{N-1} \frac{\sqrt{\omega_N^2 - \omega_p^2}}{c} l_n - \sum_{n=1}^{N-1} \frac{\sqrt{\omega_{N-1}^2 - \omega_p^2}}{c} l_n, \tag{6.13}$$

where l_n is the thickness of layer n known from previous calculation iterations. The first term is the phase imparted by layer N in the plasma stackup. The second term is the propagation phase through the lower layers of the stackup at the ω_N frequency of operation. The third term is the propagation phase through the lower layers of the stackup at the lower ω_{N-1} frequency of operation.

Using this approach, we can write a general expression for the profile reconstruction as

$$x_c(\omega_M) = x_0(\omega_0) + c \sum_{m=1}^{M} \frac{(\phi_m - \phi_{m-1}) - (\sum_{n=1}^{m-1} \frac{\sqrt{\omega_m{}^2 - \omega_{p,n}^2}}{c} l_n - \sum_{n=1}^{m-1} \frac{\sqrt{\omega_{m-1}^2 - \omega_{p,n}^2}}{c} l_n)}{\sqrt{\omega_m^2 - \omega_{m-1}^2}} \tag{6.14}$$

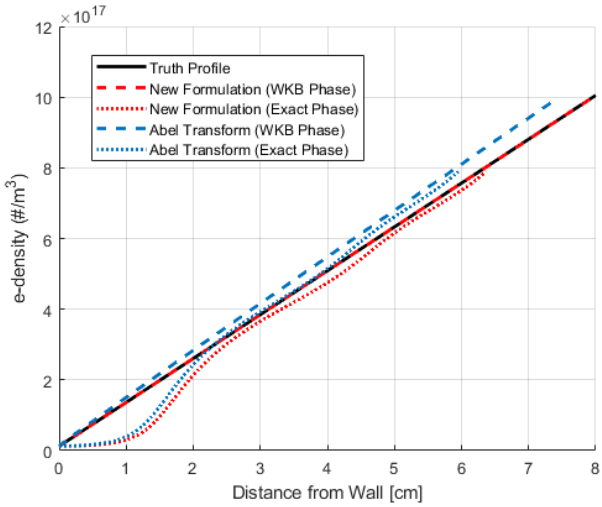

Figure 6-4. Comparing the new reconstruction formulation to the traditional Abel transform based reconstruction method.

where x_c is the position of the cutoff layer where the signal reflects for frequency ω_M. This formulation particularly accounts for the dispersive effects of the plasma. The Abel transform based formulation reported in the literature and given in Eqn. 6.4 discretized for numerical implementation is given by

$$x_c(\omega_M) = x_0(\omega_0) + \frac{c}{\pi}\sum_{m=1}^{M}\frac{\phi_m - \phi_{m-1}}{\sqrt{\omega_M^2 - \omega_{m-1}^2}}. \tag{6.15}$$

Comparing the results of the two formulations given by Eqns. 6.14 and 6.15, we can see that the expression arrived at via the Abel transform is very similar but does not account for all dispersive effects in the plasma.

The new reconstruction equation given by Eqn. 6.14 is applied to the linear electron density profile example given in Section 6.2. The results are shown in Fig. 6-4 and compared to the Abel transform approach given by Eqn 6.15. The new formulation reconstructs the truth profile very closely when the WKB approximation is entirely valid. However, we see that in reality the WKB approximation is not entirely valid leading to error in the reconstructed profile in practice.

6.4. Profile Reconstruction Using Optimization and the Analytical Solution

The analytical solution for a one-dimensional inhomogeneous plasma profile described in Section 6.1 provides a computationally efficient means to calculate the reflection from and transmission through a plasma profile. Although three-dimensional effects cannot be accounted for in the solution (e.g. three-dimensionally varying plasmas or multiple antenna apertures), the one-dimensional model can often capture the physical scenario well. The analytical approach is useful for profile reconstruction using model optimization, since a large number of optimization iterations can be

Frequency range	1 to 3 GHz, 10 MHz step
Weights $[w_1, w_2, w_3, w_4]$	[5,1,5,1]
Initial conditions $[\alpha_1, \alpha_2, \alpha_3, \alpha_4]$	[0.2 0.2 0 14]
Optimized result $[\alpha_1, \alpha_2, \alpha_3, \alpha_4]$	[4.4823 10.5597 3.4631 17.1134]
Iterations	98
Obj. function evals.	568
Total time	26s

Table 6-1. Optimization parameters and results.

calculated in a relatively short amount of time compared to full-wave solvers. The forward solve can initially be performed using an analytical calculation approach, then the optimization can later be refined using more computationally expensive full-wave approaches. As an example, we consider the 80km plasma electron density profile measured during the RAM-C2 flight experiment [6]. The reflection and transmission coefficient magnitudes and phases over a frequency range of 1 to 3 GHz are calculated for this truth profile using Eqns. 6.5 and 6.6. Although the profile electron-densities are known for this example, only the reflection and transmission coefficients are used in the reconstruction, since these are the only quantities a reflectometer would measure in practice. The plasma profile is assumed to be well-represented by a four-parameter bigaussian model given by

$$n_e(z) = \begin{cases} 10^{\alpha_4+6} \exp\left(\dfrac{-(100z-\alpha_3)^2}{\alpha_1}\right) & z < z_3 \\ 10^{\alpha_4+6} \exp\left(\dfrac{-(100z-\alpha_3)^2}{\alpha_2}\right) & z \geq z_3. \end{cases} \tag{6.16}$$

The parameters of the bigaussian model are optimized using a least squares objective function that is minimized using a constrained interior point method implemented in MATLAB. The reflection r and transmission t coefficients are a function of the four bigaussian model parameters $(\alpha_1, \alpha_2, \alpha_3, \alpha_4)$ and the frequency ω. The objective function is given by

$$\min_{\alpha_1,\alpha_2,\alpha_3,\alpha_4} \sum_{1}^{N} w_1||r|-|r_{\text{meas}}||^2 + w_2|\arg(r)-\arg(r_{\text{meas}})|^2 + w_3||t|-|t_{\text{meas}}||^2 + w_4|\arg(t)-\arg(t_{\text{meas}})|^2, \tag{6.17}$$

where N is the number of frequency points and r_{meas} and t_{meas} are the reflectometer measured reflection and transmission coefficients. For this example the weights were chosen heuristically based on comparison of the reconstructed profile to the known electron densities. However, a rigorous weighting scheme will be described in later sections. The parameters given in Table 6-1 were used to produce the optimized reconstructed profile shown in Fig. 6-5. The reflection and transmission coefficients compared to the truth are also shown in Fig. 6-5.

The reconstructed profile using the analytical expression in the forward solve visually represents the RAM-C2 80km altitude profile very well. Further tuning of the optimization allowed for a better match of the reflection and transmission coefficient magnitudes, but with the reconstructed bigaussian peak density well exceeding that of the truth profile. Although a good visual fit, the bigaussian model is not a perfect representation of the truth profile.

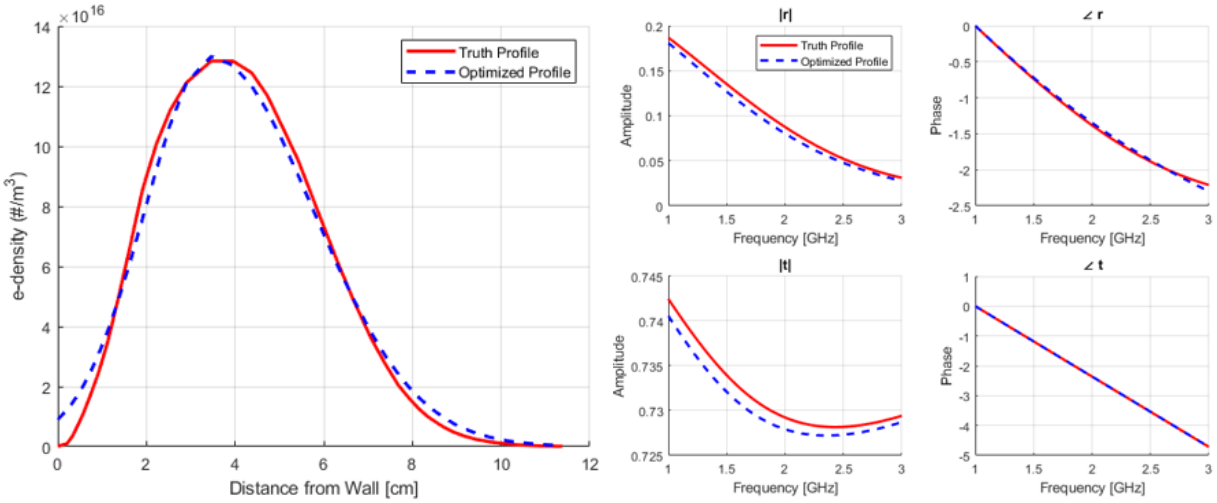

Figure 6-5. Bigaussian reconstructed electron density profile compared to the RAM-C2 80km altitude measured, truth profile.

6.5. Dakota/Empire plasma profile reconstructions

A different approach is to use a 3D forward model. As seen in the preceding sections, especially Section 5, a 3D reflectometer model may significantly differ from a 1D model for the same plasma profile — even for a 1D slab profile. We will attempt reconstruction of plasma profiles which resemble the RAM-C2 re-entry plasma, at the aft sensors, for various altitudes. The aft sensors were located $x = 3.5d_{\mathrm{N}}$ from the nosecone tip, where d_{N} is the RAM-C nose diameter. At this lateral position, the vehicle circumference is much larger than any of the microwave wavelengths under consideration. Therefore, we approximate the vehicle surface as a flat metallic plate. The plasma is represented with a 1D electron density profile $n_{\mathrm{e}}(z)$ and a uniform electron collision frequency ν. The 1D density approximation is reasonable because, at $x = 3.5d_{\mathrm{N}}$, the normal gradient of the profile is much larger than its lateral gradient.

We consider a reflectometer antenna which is an array of three identical rectangular waveguides (elements) that terminate on the ground plane at normal incidence. The major and minor dimensions of the waveguide cross sections are $a = \lambda_0$ and $b = \lambda_0/2$, respectively, where $\lambda_0 = c/f_0$ for tuning frequency $f_0 = 4$ GHz. The central waveguide (element 1) is driven by a TE_{10} sine-modulated Gaussian pulse, which excites the band from 2 GHz (waveguide cutoff) up to 7 GHz. Element 2 is offset from element 1 a distance λ_0 along the minor cross section axis and element 3 offset λ_0 along the major axis.

From the Empire time-domain solution we estimate the scattering parameters S_{11}, S_{21} and S_{31}. Twelve classes of signals (six types of measurements in in two frequency bands) are defined for use

Parameter	Min. value	Max. value	Units	Interpretation
α_1	0.1	10	[cm]	Inverse of inboard slope
α_2	1	10	[cm]	Inverse of outboard slope
α_3	0	5	[cm]	Peak density standoff distance
α_4	10	12.5	(dimensionless)	Log_{10} of peak density in inverse centimeters cubed

Table 6-2. List of the bigaussian plasma profile parameters.

in the reconstruction problem:

$$s_1(\omega) = |S_{11}| \qquad \omega \in \text{Band 1} \tag{6.18}$$
$$s_2(\omega) = \arg(S_{11}) \qquad \omega \in \text{Band 1} \tag{6.19}$$
$$s_3(\omega) = |S_{21}| \qquad \omega \in \text{Band 1} \tag{6.20}$$
$$s_4(\omega) = \arg(S_{21}) \qquad \omega \in \text{Band 1} \tag{6.21}$$
$$s_5(\omega) = |S_{31}| \qquad \omega \in \text{Band 1} \tag{6.22}$$
$$s_6(\omega) = \arg(S_{31}) \qquad \omega \in \text{Band 1} \tag{6.23}$$
$$s_7(\omega) = |S_{11}| \qquad \omega \in \text{Band 2} \tag{6.24}$$
$$s_8(\omega) = \arg(S_{11}) \qquad \omega \in \text{Band 2} \tag{6.25}$$
$$s_9(\omega) = |S_{21}| \qquad \omega \in \text{Band 2} \tag{6.26}$$
$$s_{10}(\omega) = \arg(S_{21}) \qquad \omega \in \text{Band 2} \tag{6.27}$$
$$s_{11}(\omega) = |S_{31}| \qquad \omega \in \text{Band 2} \tag{6.28}$$
$$s_{12}(\omega) = \arg(S_{31}) \qquad \omega \in \text{Band 2} \tag{6.29}$$

Frequency band 1 is $\Delta f_1 = 240$ MHz centered at $f_1 = 3$ GHz and band 2 is $\Delta f_2 = 480$ MHz centered at $f_2 = 6$ GHz.

The forward 3D problem is solved with Empire. The plasma profile in the forward problem is represented with a bigaussian profile [13] so there are four parameters,

$$n_\mathrm{e}(z) = \begin{cases} 10^{\alpha_4+6} \exp\left(\dfrac{-(100z-\alpha_3)^2}{\alpha_1}\right) & z < z_3 \\ 10^{\alpha_4+6} \exp\left(\dfrac{-(100z-\alpha_3)^2}{\alpha_2}\right) & z \geq z_3, \end{cases} \tag{6.30}$$

where z is the normal coordinate with units of meters. Interpretations and units for the bigaussian profile parameters are given in Table 6-2. Bounds for each parameter were chosen according to the microwave frequencies used in the theoretical reflectometer system and normal extent of the simulation domain ($z \in [0, 10\ \mathrm{cm}]$).

Dakota [39] drives the optimization to identify the parameterized plasma profile having a response that best fits the signal measurements. This approach to reconstructing the plasma profile is, in principle, similar to that of the V3FIT code which enjoys widespread use in the magnetic

confinement fusion community [40]. We seek the plasma profile parameters which minimize the objective function,

$$g = \boldsymbol{\epsilon}^T \Lambda \boldsymbol{\epsilon}, \tag{6.31}$$

where ϵ is the difference between the observed signals and the model signals,

$$\boldsymbol{\epsilon} = \boldsymbol{s}^{\mathrm{o}} - \boldsymbol{s}^{\mathrm{m}}. \tag{6.32}$$

In a Bayesian approach, g corresponds to the log of the likelihood; this reconstruction technique can be interpreted as a maximum likelihood optimization. The signal vectors $\boldsymbol{s}$ are organized in blocks, which each block corresponding to one of the twelve classes of signals,

$$\boldsymbol{s} = \begin{bmatrix} \boldsymbol{s}_1 \\ \boldsymbol{s}_2 \\ \vdots \end{bmatrix}. \tag{6.33}$$

In this work, the covariance matrix Λ^{-1} is taken to be a blocked diagonal matrix,

$$\Lambda^{-1} = \begin{bmatrix} \sigma_1^2 & 0 & \cdots \\ 0 & \sigma_2^2 & \cdots \\ \vdots & \vdots & \ddots \end{bmatrix}, \tag{6.34}$$

where σ_i^2 is the variance associated with the i^{th} class of signal. With Λ diagonal, g is just a sum of squares. The variances effectively weight the contribution of each class of signal in the assembly of g.

One may ask, how are values for the variances chosen? One approach is to compute signals for a sufficiently large ensemble of reasonable parameter values. The covariance matrix can be inferred from this data [41]. In this problem, however, the signals can vary greatly for different values of model parameters. We compute σ_i from the observed signals,

$$\sigma_i^2 = \frac{\sum_{k=1}^{N} \left(s_i^{\mathrm{o}}(\omega_k) - \bar{s}_i^{\mathrm{o}} \right)^2}{N} + \sigma_{i,\mathrm{noise}}^2 \tag{6.35}$$

where $\bar{s}_i^{\mathrm{o}}$ is the average value of signal class i. The contribution of white noise to the variance, $\sigma_{i,\mathrm{noise}}^2$, is to ensure a reasonable condition number for the covariance matrix. We take this to be 5% of the sample variance of the signal over the entire 5 GHz simulation result.

Because g is characterized by local minima over the allowed range of parameters, reconstruction starts with the global method DIviding RECTangles (DIRECT). In DIRECT, the global balance parameter sets how exploration of the allowed parameter range is balanced with exploitation of promising regions. We use 0.2 for the global balance parameter. After DIRECT runs for 700 iterations, the top five candidates are used as the initial point in a Newton method local optimizer. The best solution from the five local optimization runs is taken as the reconstruction result.

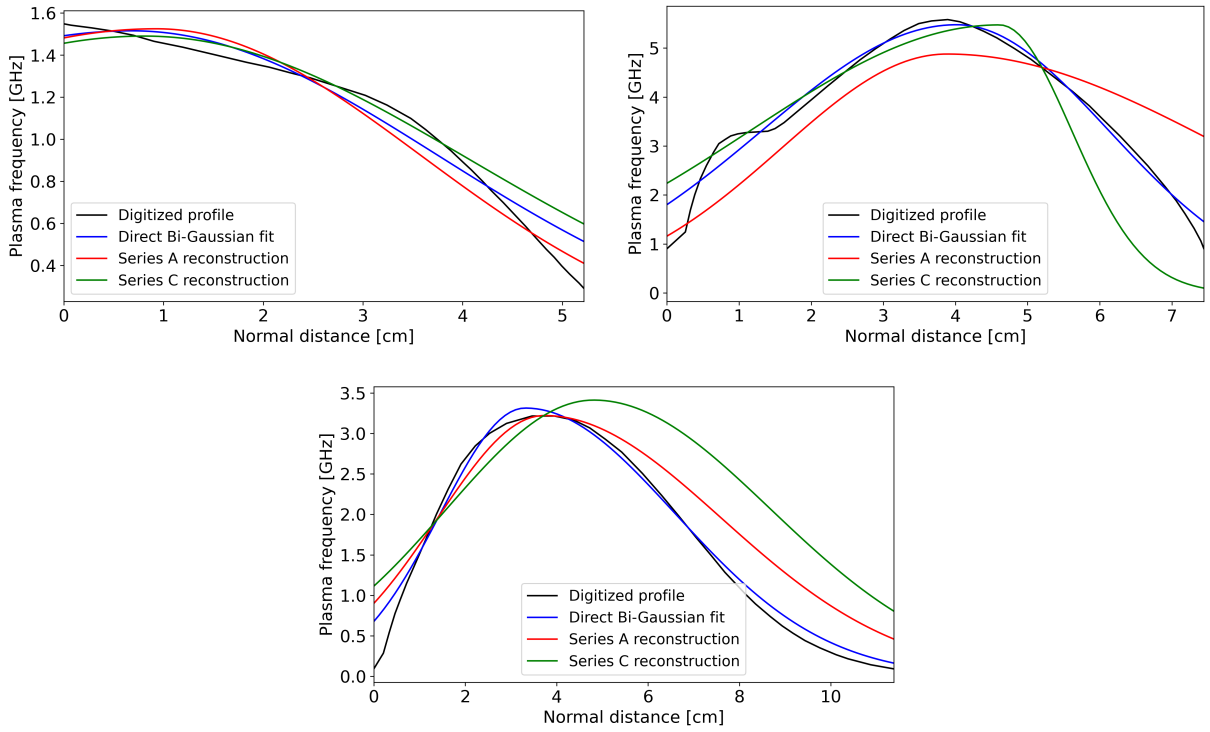

Figure 6-6. Results of the reconstructions. Reconstructions for different sets of signals are indicated, as well as straightforward bigaussian profile fits to the digitized profiles.

6.5.1. Results

We attempted to reconstruct plasma profiles based on digitizations from Schexnayder et al. [6], Fig. 14. These profiles represent the RAM-C2 re-entry plasma at different altitudes: 21.3, 53.3 and 80.2 km. We did not consider profiles at altitudes between 30 and 40 km, as the peak plasma frequencies are far above the hypothetical reflectometer maximum frequency band at 6 GHz. A reflectometer operating at higher frequencies would be required to provide diagnostics in this regime.

Four different series of reconstructions utilized different signal sets, as displayed in Table 6-3.

Series	s_1	s_2	s_3	s_4	s_5	s_6	s_7	s_8	s_9	s_{10}	s_{11}	s_{12}
Series A	✓	✓	✓	✓	✓	✓	✓	✓	✓	✓	✓	✓
Series B	✗	✗	✗	✗	✗	✗	✓	✓	✓	✓	✓	✓
Series C	✓	✓	✗	✗	✗	✗	✓	✓	✗	✗	✗	✗
Series D	✗	✗	✗	✗	✗	✗	✓	✓	✗	✗	✗	✗

Table 6-3. The signals used in each series of reconstructions.

The reconstruction results are displayed in Fig. 6-6. Bigaussian fits to the digitized electron density profiles are also shown, to demonstrate how well a bigaussian models the profiles: reasonably well for all three altitudes.

During re-entry, the boundary layer becomes turbulent when the Reynolds number exceeds some value which is dependent on the vehicle geometry. Generally, then, we expect an onset of turbulence below some altitude for a given trajectory. In our calculations, we have assumed that the boundary layer flow is laminar in all cases. However, it is known that the RAM-C2 boundary layer was turbulent below 30 km altitude. Turbulent boundary layer flow will significantly affect reflectometer S-parameters [32]. The treatment of turbulent plasma layer reflectometry is deferred to future work.

Given that we are considering the reconstruction of 1D plasma profiles over a flat plate, one may question the need for 3D electromagnetic simulations to compute the response if only a single aperture reflectometer antenna is used. A 1D calculation, however, can yield a substantially different S_{11} than 3D, depending on the plasma profile. Particularly if the plasma standoff distance is larger than or comparable to a free space wavelength [32].

As Empire is a time domain code, a single simulation yields results for all resolved frequencies within the excitation pulse. However, for the reflectometry problem we require only information for each band of the reflectometer system. Further study would benefit from the use of a frequency-domain code. However the code must provide accurate open boundary conditions for the inhomogeneous plasma-filled region. Without a plasma-matched open boundary condition, significant artificial reflections will be driven for profiles exhibiting surface wave propagation.

Future work may consider a more sophisticated parameterization than a bigaussian profile. Note that in the present case, the bigaussian profile does not fit the RAM-C2 profile at 30 km.

This page intentionally left blank.

REFERENCES

[1] RA Hartunian, GE Stewart, SD Fergason, TJ Curtiss, RW Seibold, et al. Causes and mitigation of radio frequency (RF) blackout during reentry of reusable launch vehicles. Technical report, Aerospace corporation, 2007.

[2] D. G. Swanson. *Plasma waves*. CRC Press, 2020.

[3] TK Statom. Plasma parameters from reentry signal attenuation. *IEEE Transactions on Plasma Science*, 46(3):494–502, 2018.

[4] Matthew T Bettencourt, Dominic AS Brown, Keith L Cartwright, Eric C Cyr, Christian A Glusa, Paul T Lin, Stan G Moore, Duncan AO McGregor, Roger P Pawlowski, Edward G Phillips, et al. EMPIRE-PIC: A performance portable unstructured particle-in-cell code. *Commun. Comput. Phys.*, 2021.

[5] Micah Howard, Andrew Bradley, Steven W Bova, James Overfelt, Ross Wagnild, Derek Dinzl, Mark Hoemmen, and Alicia Klinvex. Towards performance portability in a compressible CFD code. In *23rd AIAA Computational Fluid Dynamics Conference*, page 4407, 2017.

[6] Charles J Schexnayder, Paul W Huber, and John S Evans. *Calculation of electron concentration for a blunt body at orbital speeds and comparison with experimental data*. National Aeronautics and Space Administration, 1971.

[7] PW Huber, JS Evans, and CJ Schexnayder Jr. Comparison of theoretical and flight-measured ionization in a blunt body re-entry flowfield. *AIAA Journal*, 9(6):1154–1162, 1971.

[8] William L Grantham. *Flight results of a 25000-foot-per-second reentry experiment using microwave reflectometers to measure plasma electron density and standoff distance*, volume 6062. National Aeronautics and Space Administration, 1970.

[9] Jean-Claude Nédélec. Mixed finite elements in R3. *Numerische Mathematik*, 35(3):315–341, 1980.

[10] Pierre-Arnaud Raviart and Jean-Marie Thomas. A mixed finite element method for 2-nd order elliptic problems. In *Mathematical aspects of finite element methods*, pages 292–315. Springer, 1977.

[11] Duncan Alisdair Odum McGregor, Edward Love, and Richard Michael Jack Kramer. The Crank Nicolson time integrator for EMPHASIS. Technical report, Sandia National Lab.(SNL-NM), Albuquerque, NM (United States), 2018.

[12] Duncan McGregor, Edward Phillips, David Sirajuddin, and Timothy Pointon. Variational, stable, and self-consistent coupling of 3d electromagnetics to 1d transmission lines in the time domain. *Journal of Computational Physics*, 451:110856, 2022.

[13] CH Nelson. A brief history of the langley reentry communications program. *NASA special publication*, 252:1, 1971.

[14] Nicholas A Roberds, Matthew W Young, Nathan E Miller, Caleb Logemann, Tony K Statom, and Ross M Wagnild. Parasitic modulation of microwave signals by a hypersonic plasma layer. *IEEE Transactions on Plasma Science*, 2024.

[15] Devon Powell and Tom Abel. An exact general remeshing scheme applied to physically conservative voxelization. *Journal of Computational Physics*, 297:340–356, 2015.

[16] Kane S Yee, David Ingham, and Kurt Shlager. Time-domain extrapolation to the far field based on fdtd calculations. *IEEE Transactions on Antennas and Propagation*, 39(3):410–413, 1991.

[17] Raymond J Luebbers, Karl S Kunz, Michael Schneider, and Forrest Hunsberger. A finite-difference time-domain near zone to far zone transformation (electromagnetic scattering). *IEEE Transactions on Antennas and Propagation*, 39(4):429–433, 1991.

[18] MJ Barth, RR McLeod, and RW Ziolkowski. A near and far-field projection algorithm for finite-difference time-domain codes. *Journal of Electromagnetic Waves and Applications*, 6(1-4):5–18, 1992.

[19] C-C Oetting and Ludger Klinkenbusch. Near-to-far-field transformation by a time-domain spherical-multipole analysis. *IEEE Transactions on Antennas and Propagation*, 53(6):2054–2063, 2005.

[20] Torleif Martin. An improved near-to far-zone transformation for the finite-difference time-domain method. *IEEE Transactions on Antennas and Propagation*, 46(9):1263–1271, 1998.

[21] Nicholas Roberds and McGregor Duncan. A transient near to far field transformation method and verification benchmarking procedure. *Journal of Electromagnetic Waves and Applications*, 2024.

[22] Constantine A Balanis. *Antenna theory: analysis and design*. John wiley & sons, 2016.

[23] Akira Ishimaru. *Wave propagation and scattering in random media*, volume 2. Academic Press, NY, 1978.

[24] James Trolinger and William Rose. Technique for simulating and evaluating aero-optical effects in optical systems. In *42nd AIAA Aerospace Sciences Meeting and Exhibit*, page 471, 2004.

[25] John L Lumey. *Stochastic tools in turbulence*. Elsevier, 2012.

[26] Richard Michael Jack Kramer, Eric C Cyr, Sean T Miller, Edward Geoffrey Phillips, Gregg Arthur Radtke, Allen C Robinson, and John N Shadid. A plasma modeling hierarchy and verification approach. 2020.

[27] Carl Edward Rasmussen and Christopher KI Williams. *Gaussian processes for machine learning*, volume 2. MIT Press, Cambridge, 2006.

[28] Ting-i Wang and John W Strohbehn. Perturbed log-normal distribution of irradiance fluctuations. *JOSA*, 64(7):994–999, 1974.

[29] John W Strohbehn, Ting-i Wang, and James P Speck. On the probability distribution of line-of-sight fluctuations of optical signals. *Radio Science*, 10(1):59–70, 1975.

[30] Guolong He, Yafeng Zhan, Jingzhuo Zhang, and Ning Ge. Characterization of the dynamic effects of the reentry plasma sheath on electromagnetic wave propagation. *IEEE Transactions on plasma science*, 44(3):232–238, 2016.

[31] Haitao Liu, Jianfei Cai, and Yew-Soon Ong. Remarks on multi-output Gaussian process regression. *Knowledge-Based Systems*, 144:102–121, 2018.

[32] Nicholas A Roberds, Nathan E Miller, Matthew W Young, Caleb Logemann, and Ross Wagnild. An analysis of hypersonic radio blackout with Empire/SPARC. In *AIAA SCITECH 2024 Forum*, page 1645, 2024.

[33] Chul Park. *Nonequilibrium Hypersonic Aerothermodynamics*. Wiley, 1990.

[34] M Winter, M Fertig, and M Auweter-Kurtz. Status of the re-entry spectrometer system RESPECT as a payload on the european re-entry capsule EXPERT. In *4th International Symposium Atmospheric Reentry Vehicles and Systems, Arcachon, France*, 2005.

[35] Monika Auweter-Kurtz, Markus Feigl, and Michael Winter. Diagnostic tools for plasma wind tunnels and reentry vehicles at the IRS. In *Paper presented on the RTO AVT Course on" Measurement Techniques for High Enthalpy and Plasma Flows ", Rhode-Saint-Genèse, Belgium, published in RTO EN-8*, pages 25–29, 1999.

[36] NC Luhmann Jr, Henrik Bindslev, H Park, J Sanchez, G Taylor, and CX Yu. Chapter 3: microwave diagnostics. *Fusion Science and Technology*, 53(2):335–396, 2008.

[37] E Mazzucato. Microwave reflectometry for magnetically confined plasmas. *Review of Scientific Instruments*, 69(6):2201–2217, 1998.

[38] Weng Cho Chew. *Waves and fields in inhomogeneous media*. IEEE Press, 1995.

[39] Brian M Adams, Mohamed Salah Ebeida, Michael S Eldred, John Davis Jakeman, Laura Painton Swiler, John Adam Stephens, Dena M Vigil, Timothy Michael Wildey, William J Bohnhoff, John P Eddy, et al. Dakota, a multilevel parallel object-oriented framework for design optimization, parameter estimation, uncertainty quantification, and sensitivity analysis. Technical report, Sandia National Lab.(SNL-NM), Albuquerque, NM (United States), 2014.

[40] James D Hanson, Steven P Hirshman, Stephen F Knowlton, Lang L Lao, Edward A Lazarus, and John M Shields. V3FIT: a code for three-dimensional equilibrium reconstruction. *Nuclear Fusion*, 49(7):075031, 2009.

[41] Elena Sellentin and Alan F Heavens. Parameter inference with estimated covariance matrices. *Monthly Notices of the Royal Astronomical Society: Letters*, 456(1):L132–L136, 2015.

[42] George Em Karniadakis, George Karniadakis, and Spencer Sherwin. *Spectral/hp element methods for computational fluid dynamics*. Oxford University Press on Demand, 2005.

This page intentionally left blank.

APPENDIX A. Empire linear plasma model

The linear plasma model is an auxiliary differential equation, that describes a plasma that is accelerated by the electric field and slowed down by collisions. The differential equation is

$$\dot{\mathbf{j}} = \varepsilon\omega_p^2\mathbf{E} - \nu\mathbf{j}, \tag{A.1}$$

where $\mathbf{j}$ is the current produced by the plasma, ε is the permittivity of free space, ω_p is the plasma frequency, $\mathbf{E}$ is the electric field, and ν is the momentum transfer frequency. The permittivity, plasma frequency, and momentum transfer frequency are all user provided data. The plasma frequency is can be computed from the electron number density with the expression

$$\omega_p^2 = \frac{q^2 N}{m\varepsilon}, \tag{A.2}$$

where q is the electron charge, N is the electron number density, and m is the electron mass. The plasma frequency and momentum transfer frequency can vary in space but are assumed to be constant in time for the duration of the EMPIRE simulation.

The full system solved by EMPIRE is given by the linear model coupled to Ampere's and Faraday's laws,

$$\varepsilon\dot{\mathbf{E}} - \mu^{-1}\nabla\times\mathbf{B} = -\mathbf{j} \tag{A.3}$$

$$\dot{\mathbf{B}} + \nabla\times\mathbf{E} = 0 \tag{A.4}$$

$$\dot{\mathbf{j}} = \varepsilon\omega_p^2\mathbf{E} - \nu\mathbf{j} \tag{A.5}$$

Ampere's and Faraday's laws are discretized in space using compatible finite elements. The electric field, $\mathbf{E}$ is an edge function, and the magnetic field, $\mathbf{B}$ is a face field. The current from the linear plasma model exists at every volumetric quadrature point in the finite element mesh. In other words the current differential equation is evolved in time at the set of points needed to evaluate the integrated current contribution to Ampere's law.

After discretization in space the resulting system of ordinary differential equations can be integrated in time. EMPIRE integrates this system in time with the Crank-Nicolson method. The Crank-Nicolson method has several nice properties. The Crank-Nicolson method is energy conservative, which means it doesn't introduce numerical dissipation or growth into the electromagnetic waves or the plasma oscillation. It is also implicit over the plasma frequency and speed of light, which allows for timesteps larger than the plasma frequency or the speed of light CFL condition to be chosen if desired. Lastly the Crank-Nicolson method is a second order method, which means it is more accurate than a simpler first order method. The Crank-Nicolson method can be written down for the previous system as follows,

$$\frac{\varepsilon}{\Delta t}\left(\mathbf{E}^{n+1} - \mathbf{E}^n\right) - \frac{1}{2\mu}\nabla\times\left(\mathbf{B}^{n+1} + \mathbf{B}^n\right) = -\frac{1}{2}\left(\mathbf{j}^{n+1} + \mathbf{j}^n\right) \tag{A.6}$$

$$\frac{1}{\Delta t}\left(\mathbf{B}^{n+1}-\mathbf{B}^{n}\right)+\frac{1}{2}\nabla\times\left(\mathbf{E}^{n+1}+\mathbf{E}^{n}\right)=0 \tag{A.7}$$

$$\frac{1}{\Delta t}\left(\mathbf{j}^{n+1}-\mathbf{j}^{n}\right)=\frac{\varepsilon}{2}\omega_p^2\left(\mathbf{E}^{n+1}+\mathbf{E}^{n}\right)-\frac{\nu}{2}\left(\mathbf{j}^{n+1}+\mathbf{j}^{n}\right), \tag{A.8}$$

where f^n is the appropriate field at the previous time step and f^{n+1} is the field at the next time step. This is a global edge, face, and quadrature point linear system which needs to be solved. In general this system can become extremely large and difficult to solve. Fortunately EMPIRE has an efficient linear solver strategy for the edge and face system created Ampere's and Faraday's law, that can be useful for this larger system. The base linear solver strategy involves taking the Schur complement of the block system and applying a sophisticated preconditioner. The new larger system can use this linear solver if a two level Newton method is applied. A two level Newton method splits the system into two parts. In this case an initial guess for the electric field at the next time step, $\mathbf{E}_0^{n+1}$ is constructed. Generally $\mathbf{E}_0^{n+1}=\mathbf{E}^n$ is used. With this initial guess a local solve for $\mathbf{j}^{n+1}$ can be computed,

$$\frac{1}{\Delta t}\left(\mathbf{j}_0^{n+1}-\mathbf{j}^{n}\right)=\frac{\varepsilon}{2}\omega_p^2\left(\mathbf{E}_0^{n+1}+\mathbf{E}^{n}\right)-\frac{\nu}{2}\left(\mathbf{j}_0^{n+1}+\mathbf{j}^{n}\right). \tag{A.9}$$

Now with an approximate value for the current of the plasma at the next time step, the other part of the linear system can be solved using the existing linear solver,

$$\frac{\varepsilon}{\Delta t}\left(\mathbf{E}_1^{n+1}-\mathbf{E}^{n}\right)-\frac{1}{2\mu}\nabla\times\left(\mathbf{B}^{n+1}+\mathbf{B}^{n}\right)=-\frac{1}{2}\left(\mathbf{j}_0^{n+1}+\mathbf{j}^{n}\right) \tag{A.10}$$

$$\frac{1}{\Delta t}\left(\mathbf{B}^{n+1}-\mathbf{B}^{n}\right)+\frac{1}{2}\nabla\times\left(\mathbf{E}_1^{n+1}+\mathbf{E}^{n}\right)=0. \tag{A.11}$$

Since the system is linear the value $\mathbf{E}_1^{n+1}$ will be the solution to the larger fully-coupled system. So the final step is to re-solve for the current at the next time step using this value,

$$\frac{1}{\Delta t}\left(\mathbf{j}_1^{n+1}-\mathbf{j}^{n}\right)=\frac{\varepsilon}{2}\omega_p^2\left(\mathbf{E}_1^{n+1}+\mathbf{E}^{n}\right)-\frac{\nu}{2}\left(\mathbf{j}_1^{n+1}+\mathbf{j}^{n}\right). \tag{A.12}$$

The values $\mathbf{E}_1^{n+1}$, $\mathbf{B}^{n+1}$, and $\mathbf{j}_1^{n+1}$ is the solution to the original unsplit system. The two level Newton method changes a single much larger global linear solve into two local solves and a smaller global linear solve.

APPENDIX B. Notes on the Empire electromagnetic formulation and implementation

Here we provide a comprehensive look at Empire electromagnetics. This information is required in order to make any significant additions or modifications to Empire electromagnetics. Much of the language used throughout is meant to be consistent with the language used within the Empire team. An effort to concretely connect the theory to the C++ implementation is made, although it should be recognized that the implementation may or may not have been significantly refactored after the writing of these notes.

In Empire, the electric and magnetic fields are represented by basis function expansions. The electric field is represented by curl-conforming Nedelec elements,

$$\boldsymbol{E}(\boldsymbol{x},t) = \sum_{i}^{N} \sum_{j}^{N_{ned}} E_{ij}\psi_{ij}. \tag{B.1}$$

The magnetic field is represented with divergence-conforming Raviart-Thomas elements,

$$\boldsymbol{B}(\boldsymbol{x},t) = \sum_{i}^{N} \sum_{j}^{N_{rav}} B_{ij}\phi_{ij}. \tag{B.2}$$

The number of mesh cells in the computational domain is N. The cardinality of the Nedelec and Raviart-Thomas bases are N_{ned} and N_{rav} respectively. By cardinality, I mean the number of basis functions corresponding to a single mesh cell. These basis function families have certain properties which are useful and this will come up later. C^0 continuity across mesh cells is enforced for the tangential field components (for edge fields) or the normal component (for face fields). Therefore, coefficients E_{ij} and B_{ij}, for values of j which correspond to "global modes", are not independent although coefficient values for j corresponding to "interior modes" are independent. See a standard book on finite elements such as Karniadakis and Sherwin [42] for details on "global assembly" which enforces C^0 continuity. In the Empire code, *indexers* provide the information about the global assembly:

$$A_{ij} = \text{coefficientArray}_A[\ \text{indexer}_A(i,j)\ ] \tag{B.3}$$

Note that these indexers are obtained from the "DOF manager" (aka "unique global indexer" / "UGI") which is a main function of the panzer library in trilinos.

Before diving into the EM solver formulation, we have to cover important preliminaries. The Schur complement is a tool for solving linear systems where it makes sense to partition the solution vector into two or more chunks. In this case, we will be partitioning the electromagnetic solution into

an electric chunk and a magnetic chunk, since the electric and magnetic fields evolve according to different equations and are represented in different bases but are coupled. Given a "blocked" linear system,

$$X = \begin{bmatrix} A & B \\ C & D \end{bmatrix} \tag{B.4}$$

$$\begin{bmatrix} A & B \\ C & D \end{bmatrix} \begin{bmatrix} x \\ y \end{bmatrix} = \begin{bmatrix} b_1 \\ b_2 \end{bmatrix} \tag{B.5}$$

The Schur complement of D in X is,

$$S = A - BD^{-1}C \tag{B.6}$$

if $det(D) \neq 0$. The Schur complement of A in X is defined similarly in the case that $det(A) \neq 0$, but we won't use that one in the following. If D is trivial to invert, the matrix inverion lemma is a very powerful to solve the equations B.5. The solution is,

$$x = S^{-1}\left(b_1 - BD^{-1}b_2\right) \tag{B.7}$$

$$y = D^{-1}b_2 - D^{-1}CX \tag{B.8}$$

Now for the electromagnetic solver formulation. The formulation uses the solution quantities $\boldsymbol{E}$ and $\boldsymbol{B}$ (instead of, for example, the vector and scalar potentials). The evolution of the solution is described by Faraday's law and Ampere's law (instead of, for example, the second order wave equations for those quantities). If the initial conditions for $\boldsymbol{E}$ and $\boldsymbol{B}$ satisfy Gauss's law and $\nabla \cdot \boldsymbol{B} = 0$, then those conditions will always hold if $\boldsymbol{E}$ and $\boldsymbol{B}$ evolve (exactly) according to Faraday's law and Ampere's law. Within the Empire team, this fact is sometimes called an *involution*. For convenience, Faraday's law and Ampere's law are, in SI units,

$$\nabla \times \boldsymbol{E} = -\frac{\partial \boldsymbol{B}}{\partial t} \tag{B.9}$$

$$\nabla \times \boldsymbol{B} = \mu_0 \boldsymbol{J} + \epsilon_0 \mu_0 \frac{\partial \boldsymbol{E}}{\partial t}. \tag{B.10}$$

The multidimensional Newton method is used to solve these equations. The reason for this approach is because it readily extends to nonlinear systems. Thus, in principle, the addition of a nonlinear material model to Empire would be trivial. To proceed with a Newton method formulation, we define the residuals,

$$0 = \boldsymbol{F}_1(\boldsymbol{E}, \boldsymbol{B}) = \epsilon_0 \dot{\boldsymbol{E}} - \frac{1}{\mu_0} \nabla \times \boldsymbol{B} + J \tag{B.11}$$

$$0 = \boldsymbol{F}_2(\boldsymbol{E}, \boldsymbol{B}) = \nabla \times \boldsymbol{E} + \dot{\boldsymbol{B}} \tag{B.12}$$

Then we do a Taylor series expansion of the residual,

$$\boldsymbol{F}_1(\boldsymbol{E}^n + \Delta\boldsymbol{E}, \boldsymbol{B}^n + \Delta\boldsymbol{B}) = \boldsymbol{F}_1(\boldsymbol{E}^n, \boldsymbol{B}^n) + \frac{\partial \boldsymbol{F}_1}{\partial \boldsymbol{E}} \Delta\boldsymbol{E} + \frac{\partial \boldsymbol{F}_1}{\partial \boldsymbol{B}} \Delta\boldsymbol{B} \tag{B.13}$$

$$\boldsymbol{F}_2(\boldsymbol{E}^n + \Delta\boldsymbol{E}, \boldsymbol{B}^n + \Delta\boldsymbol{B}) = \boldsymbol{F}_2(\boldsymbol{E}^n, \boldsymbol{B}^n) + \frac{\partial \boldsymbol{F}_2}{\partial \boldsymbol{E}} \Delta\boldsymbol{E} + \frac{\partial \boldsymbol{F}_2}{\partial \boldsymbol{B}} \Delta\boldsymbol{B} \tag{B.14}$$

The equations B.13 and B.14 are arranged into a blocked matrix form,

$$\underbrace{\begin{bmatrix} \frac{\partial \boldsymbol{F}_1}{\partial \boldsymbol{E}} & \frac{\partial \boldsymbol{F}_1}{\partial \boldsymbol{B}} \\ \frac{\partial \boldsymbol{F}_2}{\partial \boldsymbol{E}} & \frac{\partial \boldsymbol{F}_2}{\partial \boldsymbol{B}} \end{bmatrix}}_{\text{Jacobian matrix}} \underbrace{\begin{bmatrix} -\Delta \boldsymbol{E} \\ -\Delta \boldsymbol{B} \end{bmatrix}}_{\text{solution/increment}} = \underbrace{\begin{bmatrix} F_1(\boldsymbol{E}^n, \boldsymbol{B}^n) \\ F_2(\boldsymbol{E}^n, \boldsymbol{B}^n) \end{bmatrix}}_{\text{residual/RHS}} \tag{B.15}$$

so we can utilize the Schur complement which will allow us to solve a smaller linear system with the Krylov space solver. Solving this linear system is one step of the Newton method and only one step is needed since it is a linear system. However, it clearly follows from equation B.12 that the lower-right block of the Jacobian matrix is the identity matrix. Therefore, we should use the Schur complement matrix inversion lemma to invert this system since inversion of the lower-right block is trivial.

We now need explicit expressions for the Jacobian matrix element values. This requires fully discretizing equations B.9 and B.10. Let's start with spatially discretizing Ampere's law. Obtain the weak form (spatially discretized) version of Ampere's law by multiplying by a test function ψ_i and integrating,

$$\int \psi_i \cdot (\epsilon \dot{\boldsymbol{E}})\, dV - \int \psi_i \cdot \frac{1}{\mu_0} \nabla \times \boldsymbol{B}\, dV + \underbrace{\int \psi_i \cdot \boldsymbol{J}\, dV}_{\text{integrated current}} = 0 \tag{B.16}$$

Note that the third term is referred to, throughout the Empire code, as the "integrated current". Since we choose the test functions to be the electric field expansion functions ψ_i this is a Galerkin method. We now write equation B.16 in terms of the mass matrices,

$$M_D \dot{\boldsymbol{E}} - \underbrace{C^T M_H}_{\text{weak curl}} \boldsymbol{B} + \underbrace{M_E \boldsymbol{J}}_{\text{integrated current}} = 0 \tag{B.17}$$

where M_D is the edge mass matrix times ϵ_0, M_H is the face mass matrix times $1/\mu_0$, M_E is the edge mass matrix and C is the strong curl operator. $C^T M_H$ is referred to as the "weak curl". The strong curl operating on an edge field will give the curl of that field, while a weak curl operating on a face field will give the integrated curl of that field.

Now let's spatially discretize Faraday's law. Because of the choice of basis functions for representing $\boldsymbol{E}$ and $\boldsymbol{B}$, the discretized Faraday's law is in strong form (not weak form as for Ampere's law above):

$$C\boldsymbol{E} + \dot{\boldsymbol{B}} = 0 \tag{B.18}$$

Now temporally discretize Faraday's and Ampere's laws.

$$\alpha M_D(\boldsymbol{E}^{n+1} - \boldsymbol{E}^n) - C^T M_H\Big(\beta \boldsymbol{B}^{n+1} + (1-\beta)\boldsymbol{B}^n\Big) + M_E \boldsymbol{J}^n = \boldsymbol{F}_1 \tag{B.19}$$

$$C(\beta \boldsymbol{E}^{n+1} + (1-\beta)\boldsymbol{E}^n) + \alpha(\boldsymbol{B}^{n+1} - \boldsymbol{B}^n) = \boldsymbol{F}_2 \tag{B.20}$$

where $\alpha = 1/\Delta t$ and β is a parameter which presumably varies at each time step according to the chosen Runge-Kutta scheme. With these expressions for the fully discretized residual, the Jacobian matrix in equation B.15 can be written,

$$\mathcal{J} = \begin{bmatrix} \alpha M_D & -\beta C^T M_H \\ \beta C & \alpha \mathbb{I}_B \end{bmatrix} \tag{B.21}$$

where $\mathbb{I}_B$ is the face-field identity matrix. Note that anywhere in the Empire code, the operators $\mathbb{I}_B$, M_H, M_E, C, $C^T M_H$, M_D and other useful linear operators are available, from the "Linear Operator Manager".

In the code, the Jacobian matrix is stored in x_matrix and x_dot_matrix:

$$\mathcal{J} = \beta X + \alpha \dot{X} \tag{B.22}$$

The x_matrix and x_dot_matrix are defined,

$$X = \begin{bmatrix} 0 & -C^T M_H \\ C & 0 \end{bmatrix} \tag{B.23}$$

$$\dot{X} = \begin{bmatrix} M_D & 0 \\ 0 & \mathbb{I}_B. \end{bmatrix} \tag{B.24}$$

These definitions are useful because they can also be used to compute the residual. Indeed, the code computes the residual in the following way,

$$X \begin{bmatrix} \boldsymbol{E} \\ \boldsymbol{B} \end{bmatrix} + \dot{X} \begin{bmatrix} \dot{\boldsymbol{E}} \\ \dot{\boldsymbol{B}} \end{bmatrix} = \begin{bmatrix} \boldsymbol{F}_1 - \boldsymbol{J} \\ \boldsymbol{F}_2 \end{bmatrix} \tag{B.25}$$

The current is added in a separate step. Rows associated with boundary conditions are, of course, treated differently. In the code, these matrices are constructed in the *setupMatrices* function of the *ElectromagneticSolverInterface*, which is called during initialization. The mass matrices and curl operators are also constructed and registered with the linear operator manager in *setupMatrices*.

In this scheme for solving for $\Delta \boldsymbol{E}$ and $\Delta \boldsymbol{B}$, there are two residuals to speak of. On one hand, we have the residual,

$$R = \begin{bmatrix} \boldsymbol{F}_1 \\ \boldsymbol{F}_2 \end{bmatrix}. \tag{B.26}$$

This residual is assembled in the *ElectroMagneticSolverInterface::evaluateResidual* method. There is also the residual associated with the Schur complement matrix inversion trick. From Eqs. B.5, B.7, B.11, B.12 and B.5, this residual is,

$$\mathcal{R} = b_1 - B D^{-1} b_2 \tag{B.27}$$

$$= F_1 - (-\beta C^T M_H)(\alpha \mathbb{I}_B)^{-1} F_2 \tag{B.28}$$

$$= F_1 + \frac{\beta}{\alpha} C^T M_H \mathbb{I}_B^{-1} F_2 \tag{B.29}$$

This "Schur complement trick residual" is assembled in *ElectroMagneticSolverInterface::forwardSolveResidual_* method.

DISTRIBUTION

Email—Internal

Name	Org.	Sandia Email Address
Technical Library	1911	sanddocs@sandia.gov

Hardcopy—Internal

Number of Copies	Name	Org.	Mailstop
1	L. Martin, LDRD Office	1910	0359

Sandia National Laboratories

Sandia National Laboratories is a multimission laboratory managed and operated by National Technology & Engineering Solutions of Sandia LLC, a wholly owned subsidiary of Honeywell International Inc., for the U.S. Department of Energy's National Nuclear Security Administration under contract DE-NA0003525.